Multi-compartmental model of glymphatic clearance of solutes in brain tissue

Alexandre Poulain, Jørgen Riseth, Vegard Vinje

Multi-compartmental model of glymphatic clearance of solutes in brain tissue

Alexandre Poulain*† Jørgen Riseth ‡ Vegard Vinje §

September 27, 2022

Abstract

The Glymphatic system is the subject of numerous pieces of research in Biology. Mathematical modeling plays a considerable role in this field since it can indicate the possible physical effects in this system and validate the biologists' hypotheses. The available mathematical models that describe the system at the scale of the brain (*i.e.* the macroscopic scale) are often solely based on the diffusion equation and do not consider the fine structures formed by the perivascular spaces. We therefore propose a mathematical model representing the time and space evolution of a mixture flowing through multiple compartments of the brain. We adopt a macroscopic point of view in which the compartments are all present at any point in space. The equations system is composed of two coupled equations for each compartment: One equation for the pressure of a fluid and one for the mass concentration of a molecule. The fluid and solute can move from one compartment to another according to certain membrane conditions modeled by transfer functions. We propose to apply this new modeling framework to the clearance of ^{14}C-inulin from the rat brain.

1 Introduction

The proposed glymphatic system [32] explains the clearance of metabolic waste from the brain and has been the subject of many pieces of research in the past decade [29, 1, 34]. The glymphatic theory suggests that clearance of metabolic solutes in the brain is facilitated by specific pathways for exchange between interstitial fluid (ISF) and cerebrospinal fluid (CSF). This exchange occurs via perivascular spaces (PVSs), that are small fluid filled spaces surrounding blood vessels. According to the glymphatic theory, CSF enters the parenchyma via periarterial spaces and exits it via perivenous spaces. Furthermore, Iliff *et al.* [32] suggested that a bulk flow of fluid occurs in the interstitial space between periarterial and perivenous spaces draining metabolic waste out of the brain. Understanding the glymphatic system is critically important since its impairment may be linked to neurodegenerative diseases such as Alzheimer's decease [62].

Even after a decade of research to verify this theory many questions remain to be answered: *i)* Does the circulation of CSF as described by Iliff *et al.* [32] (inflow around arteries and outflow around veins) really occur? *ii)* What are the mechanisms explaining the movement of CSF in the perivascular spaces? *iii)* Does convection in the interstitial space occur and is this flow sufficient to dominate transport?

*Department for Numerical Analysis and Scientific Computing, Simula Research Laboratory, Oslo, Norway
†Email: poulain@simula.no
‡jorgennr@simula.no
§vegard@simula.no

In vivo studies using two-photon microscopy have imaged flow along periarterial spaces at the pial surface in the same direction as blood [9, 47], suggesting these spaces act as an entry to the brain. However, the direction and magnitude of flow in penetrating PVS is still debated [7]. Futhermore, the question of the existence of a bulk flow of fluid within the extracellular space (ECS) as proposed by Iliff *et al.* [32] remains open. Indeed, some pieces of research indicate that solute transport in the ECS is dominated by diffusion [4, 29, 69], while others claim that diffusion alone can not explain the transport of tracer within the brain [75, 61]. In a recent study, Ray *et al.* [60] concluded that transport of large molecules is dominated by convection given the expected ECS flow rates reported in the literature. Convection-diffusion equations have been widely used to study transport within the brain [60, 75, 29, 53, 71, 61, 14]. These works helped gain some insights into the relevant mechanisms that may play a role for clearance of interstitial solutes. However, in these works, the fluid velocities and concentrations are averaged between ECS and PVS (and all other routes of transport) to capture the overall spread of solutes.

In contrast, multiple-compartment models that can distinguish between different compartments such as blood vessels and tissue have been used to study for example drug transport to the lung [22] or clot fragmentation [19] with great detail. However, these models require detailed information on vessel structure and require too many degrees of freedom to study the brain at the macroscale.

To circumvent these limitations, homogenized models have been successfully applied to represent infiltration in porous media [31]. Such framework has been successfully applied to represent transport of solute and fluid in the ECS and vascular network of vascularized tumors [67, 68, 57]. In full scale patient-specific geometries, multiple-network poroelastic theory (MPET) have been used to study exchange between multiple fluid compartments contained within the (elastic) brain tissue [10, 11, 5, 74, 76, 27, 26]. However, the MPET equations have not yet been investigated in terms of transport of tracers or solutes in the context of the glymphatic system.

In this paper, we therefore develop a homogenized model to describe the glymphatic system and the blood flow at the scale of the rat brain (Figure 1). To validate the relevancy of our modelling framework, we study the clearance of the molecule ^{14}C-inulin from the rat brain. In particular, the presented multi-compartment model represents movement of CSF through different structures including the subarachnoid space (SAS), the PVSs, the ECS and the blood vascular tree. This modeling of the fluid movement is coupled to diffusion-convection equations for each compartment to represent the clearance of ^{14}C-inulin from the brain. Our model suggests that without blood filtration, transport is explained mainly by diffusion within the brain. However, when ISF is allowed to filtrate across the vascular wall, PVS flow was reversed and clearance from the ECS substantially increased.

2 Methods

2.1 Mathematical models

Notations We denote by $\Omega \subset \mathbb{R}^3$ the spatial domain, *i.e.* the rat brain. We assume that the boundary $\partial\Omega$ of this domain is sufficiently smooth. Therefore, we denote by $\mathbf{x} \in \Omega$, any point of this domain such that the coordinates are given by $\mathbf{x} = (x_1, x_2, x_3)$. We emphasize that, in the rest of this article, to denote vectors, we use bold symbols. Since we model the time evolution of the glymphatic system, our time-space domain is denoted by $\Omega_T = \Omega \times [0, T]$, with $T > 0$ a finite time. We test two different mathematical models: First, a pure diffusion model in a single compartment and then a multi-compartment model which includes both diffusive and convective transports. We use the following notation convention: when an unknown or a parameter is indicated with a subscript, it denotes its compartment. The subscripts a, c and v are used to

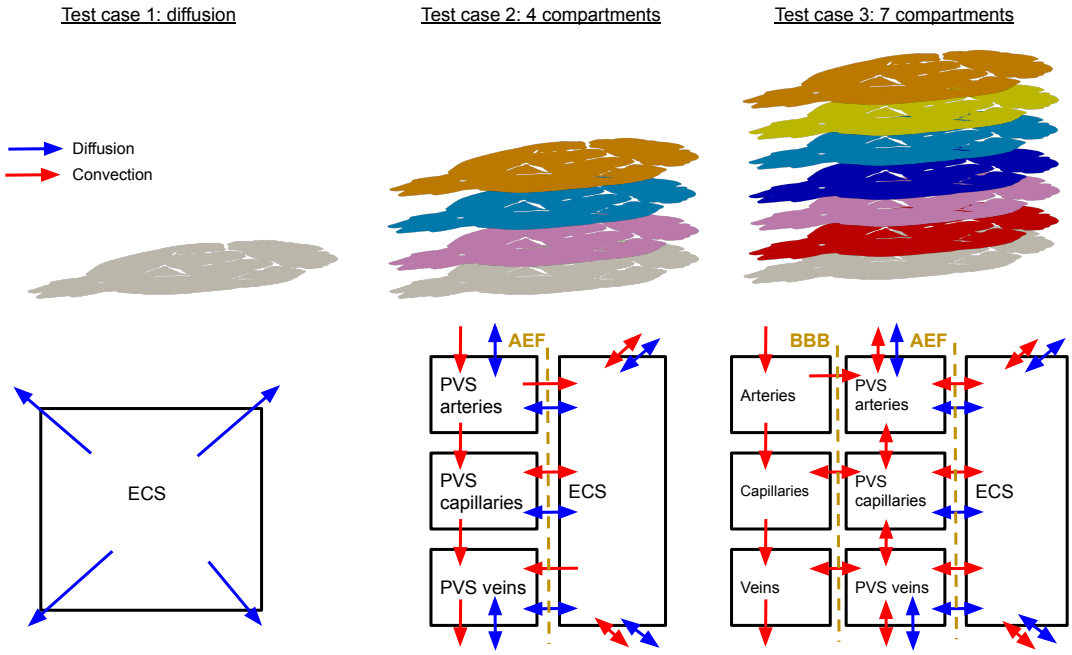

Figure 1: Illustrative representation of the three test cases. Red arrows indicate the movement of fluids through the compartments and blue arrows the diffusive movement of ^{14}C-inulin . Double arrows indicate that the movement could be directed in both directions and is, a priori, not known. With exception of the blood compartments, the arrows pointing to the outside of any compartment denotes a connection of this compartment with the subarachnoid space. *AEF* denotes the *astrocyte endfeet barrier* and *BBB* the *blood-brain barrier*.

denote the arterial, capillary and venous blood networks, respectively. Similarly, the subscripts pa, pc, pv are used to denote the periarterial, pericapillary and perivenous fluid networks. The subscript e indicates the ECS.

The diffusion equation Denoting by $c_e = c_e(t, \mathbf{x})$ the solute concentration in ISF, the diffusion equation reads

$$\frac{\partial c_e}{\partial t} = D_e^* \Delta c_e, \quad \forall \mathbf{x} \in \Omega, \quad t \in (0, T]. \tag{1}$$

Here, D_e^* is the effective diffusion coefficient of the molecule in the ECS.

The multi-compartment model To take into account the different structures in which the fluid flows, we consider the multiple compartments as depicted in the schematic illustrations given in Fig 1. We denote by J the set of compartments (J can thus be modified to describe all three test cases shown in Fig 1) and we denote the pressure in the $j-$th compartment by $p_j = p_j(t, \mathbf{x})$ and for the solute concentration $c_j = c_j(t, \mathbf{x})$. The fluid flow in our model is computed via static MPET equations [6, 74] without displacements. We denote by ϕ_j the porosity of the $j-$th compartment (*i.e.* the relative volume taken by the pores of this compartment). We emphasize that the compartments are all present at any point $\mathbf{x} \in \Omega$. Thus, under the assumption of incompressible flow, for all $\mathbf{x} \in \Omega$, $t \in (0, T]$, we have the equations' systems, for each $j \in J$

$$\begin{cases} -\nabla \cdot (\frac{\kappa_j}{\phi_j \mu_j} \nabla p_j) = r_j, \\ \dfrac{\partial c_j}{\partial t} - \dfrac{\kappa_j}{\phi_j \mu_j} \nabla \cdot (c_j \nabla p_j) - D_j^* \Delta c_j = s_j. \end{cases} \tag{2}$$

Here, κ_j is the permeability coefficient of the fluid, μ_j is the dynamic viscosity of the fluid, D_j^* is the effective diffusion coefficient in the j-th compartment, and r_j, s_j are the transfer functions to model the exchanges between the compartments and will be described in the next paragraph.

Remark 1. *For simplicity reasons, we consider the porosity, permeability and diffusion coefficients to be isotropic,* i.e. *no spatial variation are considered for these parameters.*

Remark 2. *We note that c_j denote the microscopic fluid concentrations, which is related to the macroscopic or total concentration via $c_j^{total} = c_j * \phi_j$.*

Transfer functions The transfer functions in System (2) model the exchange of fluid, r_j, and solutes, s_j, between the different compartments. These compartments are separated by a membrane or are in communication with other vessels along the same tree (*e.g.* an artery branching to capillaries or the PVS around arteries branching to the PVS around capillaries).

When the compartments are separated by a membrane, the fluid flows from one compartment to another due to a difference of pressure which is related to the hydraulic conductivity of the membrane, *i.e.*

$$r_j = \frac{1}{\phi_j} \sum_{i \in J, i \neq j} \gamma_{j,i} \left[(p_i - p_j) - \sigma_{i,j} (\pi_i - \pi_j) \right], \tag{3}$$

with

$$\gamma_{j,i} = L_{i,j} \frac{|S_{i,j}|}{|\Omega|}, \tag{4}$$

where $|\Omega| = \int_\Omega 1 \, \mathrm{d}\mathbf{x} = 2313 \text{ mm}^3$ is the brain volume, $L_{i,j}$ is the hydraulic conductivity of the membrane separating the $i-$th and $j-$th compartments, $\frac{|S_{i,j}|}{|\Omega|}$ is the ratio between the surface

of the membrane and the total volume of the tissue, and $\sigma_{i,j}$ is the osmotic reflection coefficient for the membrane. This reflection coefficient corresponds to a specific solute. In this work, we only consider osmotic effects due to plasma cells in the blood where π_j is the osmotic pressure. The solute crosses the membrane due to the combination of two effects: Either via convection of fluid through the pores of the membrane or via diffusion. These two effects are modelled by the transfer functions (see *e.g.* [33])

$$s_j = \frac{1}{\phi_j} \sum_{i \in J, i \neq j} \lambda_{j,i}(c_i - c_j) + \frac{(c_j + c_i)}{2} \tilde{\gamma}_{j,i}(p_i - p_j - \sigma_{i,j}(\pi_i - \pi_j)), \tag{5}$$

where this time

$$\lambda_{j,i} = P_{i,j} \frac{|S_{i,j}|}{|\Omega|}, \quad \tilde{\gamma}_{j,i} = \gamma_{j,i}(1 - \sigma_{\text{reflect}}),$$

in which $P_{i,j}$ is the permeability of the membrane separating the $i-$th and $j-$th compartments to the solute and σ_{reflect} reflects the solvent-drag reflection coefficient.

In the case of a continuous transition between compartments (e.g. between arteries and capillaries), no membrane is present (and we thus set $P_{i,j} = 0$). We provide in Subsection 2.3 values for the exchange coefficients $\gamma_{j,i}, \tilde{\gamma}_{j,i}, \lambda_{j,i}$.

Clearance of ^{14}C-inulin To study the clearance of ^{14}C-inulin from the rat brain, we consider 3 variations.

We first assume that bulk flow of fluid in the interstitial space is negligible, and transport occurs due to diffusion in the interstitial space only. Hence, we use Equation (1). Clearance of ^{14}C-inulin occurs at the brain surface and is modelled by appropriate boundary conditions that are described below. This scenario is represented by Test case 1 on Fig 1.

Secondly, we consider a clearance of ^{14}C-inulin due to the glymphatic system. Hence, we use System (2) with $|J| = 4$ compartments: ECS, PVS around arteries, PVS around capillaries, and PVS around veins. Test case 2 in Fig 1 depicts this scenario. CSF is assumed to flow from the PVS around arteries to the PVS around capillaries or in the ECS. From the PVS around capillaries, CSF flows to the ECS or to the PVS around veins. From the ECS, CSF may be reabsorbed in the PVS around veins or capillaries. Clearance from the brain may occur at the brain surface from the ECS, the PVS around veins and the PVS around arteries.

Thirdly, we add the effect of the blood vasculature. Indeed, cerebral blood vessels are not impermeable and some fluid could leak from them to the other structures [54]. This case is depicted by Test case 3 in Fig 1.

For the sake of clarity, in the following we refer to these 3 applications of our modeling framework as

- **Pure diffusion model: Test case 1.** Diffusion only in the interstitial space modeled by Equation (1).
- **4-compartment model: Test case 2.** Clearance from the glymphatic system using System (2) with $J = 4$ compartments.
- **7-compartment model: Test case 3.** Clearance from the glymphatic system and considering the blood perfusion that could affect fluid movement using System (2) with $J = 7$ compartments.

2.2 Initial and boundary conditions

Initial condition We consider the application in which the solute is injected directly into the ECS of the rat brain, and assume that the initial ^{14}C-inulin concentration is given as a three-dimensional Gaussian around the center of injection $\mathbf{s}$ (see Fig 2b),

$$c_e(0,\mathbf{x}) = C^0 \exp \frac{|\mathbf{x}-\mathbf{s}|^2}{\sigma^2} \tag{6}$$

where $C^0 = 1.0$ is a reference concentration, and σ determines the initial spread of the solute after injection. The reference concentration is chosen such that the integral of the initial condition over the domain matches the injected tracer amount. We emphasize that the initial condition is the same for the case of a single compartment and when multiple compartments are considered. In the following, we present numerical results for which the initial point of injection is located in the right hemisphere with coordinates $\mathbf{s} = (4, 2, 3)$.

Boundary conditions To generate a relevant bulk flow within the PVSs, we assume a slight pressure difference between the boundary of the PVSs around arteries and veins. We know that intracranial pressure in rat is 4 ± 0.74mmHg (see [64]). ISF pressure has been measured in rat [79] and is 3.43 ± 0.65mmHg.

Therefore, we supplement the pressure equations with

$$\begin{cases} -\frac{\kappa_e}{\mu_{\text{CSF}}} \frac{\partial p_e}{\partial \boldsymbol{\nu}}(t,\mathbf{x}) = L_{e,SAS}(p_{\text{SAS}} - p_e), \quad -\frac{\kappa_{pa}}{\mu_{\text{CSF}}} \frac{\partial p_{pa}}{\partial \boldsymbol{\nu}}(t,\mathbf{x}) = L_{\text{PVSpial},pa}(p_{\text{PVSpial}} - p_{pa}), \\ \frac{\partial p_{pc}}{\partial \boldsymbol{\nu}}(t,\mathbf{x}) = 0, \quad p_{pv} = 3.36\,\text{mmHg}, \end{cases} \tag{7}$$

on $\partial\Omega$, $t > 0$, with $\boldsymbol{\nu}$ being the outward normal vector to the boundary $\partial\Omega$ and $p_{\text{PVSpial}} = 4.74$mmHg is the CSF pressure inside the PVS of pial arteries and $p_{\text{SAS}} = 3.74$mmHg is the CSF pressure inside the SAS. The coefficients $L_{\text{PVSpial},pa}$ and $L_{SAS,e}$ are related to the permeability of the pial surface of the brain for the CSF.

Considering the cerebral blood perfusion (test case 3), fluid movement is affected and we need additional parameters, namely

$$\begin{cases} -\frac{\kappa_a}{\mu_a} \frac{\partial p_a}{\partial \boldsymbol{\nu}}(t,\mathbf{x}) = L_{a,blood}(p_{\text{blood}} - p_a), \\ \frac{\partial p_c}{\partial \boldsymbol{\nu}}(t,\mathbf{x}) = 0, \quad p_v(t,\mathbf{x}) = 7.0\,\text{mmHg}, \end{cases} \quad \text{on } \partial\Omega,\ t \geq 0, \tag{8}$$

with $p_{\text{blood}} = 120\,\text{mmHg}$ (see [28]).

For the concentration equations, different boundary conditions are considered. The first and simplest approach is to use homogeneous Dirichlet boundary conditions to represent clearance from the tissue and zero-flux boundary conditions for the compartments that are not in communication with the SAS. Namely, we impose Dirichlet boundary conditions for the concentration equations in the periarterial, perivenous and extracellular spaces since these compartments represent possible outflow routes. For the other compartments we assume that there is no flow at the surface of the brain. Thus, we have

$$\begin{cases} c_j\big|_{\partial\Omega} = 0, \quad \text{for} \quad j = \{pa, pv, e\}, \\ \frac{\partial\left(D_j \nabla c_j + \frac{\kappa_j}{\mu_j} c_j \nabla p_j\right)}{\partial \nu} = 0 \quad \text{on } \partial\Omega, \text{ and for } j = \{pc\}. \end{cases}$$

This condition assumes that no membrane restricts ^{14}C-inulin movement over the pial surface. Moreover, the clearance of solutes from the SAS is assumed to be sufficiently quick, so that ^{14}C-inulin concentration in the CSF stays zero.

Alternatively, the solute concentration in the CSF within the SAS may be represented by a time-dependent boundary condition. Still assuming instant absorption at the surface, we modify the Dirichlet boundary conditions to

$$c_j\big|_{\partial\Omega} = g(t), \quad \text{for} \quad j = \{pa, pv, e\}, \quad t > 0, \tag{9}$$

where $g(t)$ is given as the total amount of molecules that has been cleared from the brain up to that time, averaged over the CSF volume V_{CSF} in the fluid filled space surrounding the brain, *i.e.* the SAS. The rate of change of molecules tracer within the brain, per unit of time, is given by

$$\frac{d}{dt}\int_\Omega \sum_{j\in J} \phi_j c_j \, \mathrm{d}\mathbf{x} = \sum_{j\in J}\int_\Omega \phi_j \frac{\partial c_j}{\partial t} \, \mathrm{d}\mathbf{x} = -\int_{\partial\Omega} \mathbf{q}\cdot\boldsymbol{\nu} \, \mathrm{d}s, \tag{10}$$

in which $\mathbf{q}$ is the mass total flux from all the compartments at the surface of the brain (we recall that $\boldsymbol{\nu}$ is the outward pointing normal to the surface of the brain). For each compartment this flux is given by the combination of diffusion and convection

$$\mathbf{q} = \sum_{j\in J} -D_j\nabla c_j + c_j\mathbf{v}_j, \quad \mathbf{v}_j = -\frac{\kappa_j}{\mu_j}\nabla p_j.$$

A decrease of molecules within the brain, corresponds to an increase of concentration in the SAS, and vice-versa. Therefore, g satisfies the linear ordinary differential equation

$$\begin{cases} \frac{dg}{dt} & = -\alpha g(t) + \frac{1}{V_{\text{CSF}}}\int_{\partial\Omega}\mathbf{q}\cdot\boldsymbol{\nu}\,\mathrm{d}s, \\ g(0) & = 0, \end{cases} \tag{11}$$

where $\alpha > 0$ is the rate of CSF absorption from the SAS. This model assumes instantaneous absorption of molecules in the CSF, and instant mixing of the solute within the whole SAS.

If $\alpha = 0$, the latter Dirichlet boundary condition may be interpreted as a model for conservation of the amount of molecules. Thus, assuming that the molecules are not eliminated from the SAS, an alternate formulation of this condition is given by

$$\sum_{j\in J}\int_\Omega \phi_j c_j \, \mathrm{d}x + g(t)V_{\text{CSF}} = N_0, \tag{12}$$

where $N_0 = \sum_{j\in J}\int_\Omega \phi_j c_j(0,\mathbf{x}) \, \mathrm{d}x$ is the total amount of molecules initially injected into the brain. Thus, this time g is simply given by

$$g(t) = \frac{1}{V_{\text{CSF}}}\left(N_0 - \sum_{j\in J}\int_\Omega \phi_j c_j \, \mathrm{d}\mathbf{x}\right). \tag{13}$$

We test the effect of all three different concentration boundary conditions (Homogeneous, Conservation (9) with Equation (13), and Decay (9) with Equation (11)) on clearance of ^{14}C-inulin from the brain.

2.3 Parameter values

2.3.1 For the convection-diffusion equation

^{14}C-inulin diffusion coefficient The free diffusion coefficient for ^{14}C-inulin is $D_{\text{free}} = 2.98 \times 10^{-4}\,\text{mm}^2/\text{s}$ as reported in [40], and the tortuosity of the rat brain is given by $\lambda = 1.7$ (see [78]). Hence, the effective diffusion coefficient of ^{14}C-inulin in the rat brain is given by

$$D^* = \frac{D_{\text{free}}}{\lambda^2} = 1.03 \times 10^{-4}\,\text{mm}^2/\text{s}.$$

2.3.2 For the multi-compartment model

Porosity coefficients From [15], we know that the volume fraction of the extracellular space of rats is

$$\phi_e = 0.14.$$

From [58], the volume fraction of blood is estimated to be

$$V_{\text{Blood}} = 3.29 \times V_{\text{Brain}}/100.$$

Furthermore, using the fractions of arteries, veins, and capillaries stated in [41], we obtain

$$\phi_a = 0.00658, \quad \phi_c = 0.00329, \quad \phi_v = 0.02303.$$

The porosity of the PVS in human is estimated to $V_{\text{PVS}} \approx 0.3 \times V_{\text{Brain}}/100$ (see *e.g.* [8]). This value is unknown for the rat, hence, we assume that the relation holds without relying on measurements. From the estimated percentages of arterial, venous, and capillary blood volume, we estimate

$$\phi_{pa} = 0.0006, \quad \phi_{pc} = 0.0003, \quad \phi_{pv} = 0.0021.$$

Fluid parameters The interstitial fluid and plasma in the blood compartments are assumed to possess different properties. The dynamic viscosity of blood and CSF is given by respectively [26] and [12]. We have

$$\mu_a = \mu_v = \mu_c = 2.67 \times 10^{-3}\,\text{Pa s}, \text{ and } \mu_{pa} = \mu_{pv} = \mu_{pc} = \mu_e = 7.0 \times 10^{-4}\,\text{Pa s}.$$

In [77], the authors used experimentally obtained resistance coefficients for several compartments. From the definition of these resistances, we can compute the following permeability coefficients (see Appendix A for details).

$$\begin{aligned}
&\kappa_a = 3.30 \times 10^{-6}\,\text{mm}^2, \quad \kappa_v = 6.59 \times 10^{-6}\,\text{mm}^2, \quad \kappa_c = 1.14 \times 10^{-9}\,\text{mm}^2,\\
&\kappa_{pa} = 1.0 \times 10^{-11}\,\text{mm}^2, \quad \kappa_{pv} = 6.51 \times 10^{-9}\,\text{mm}^2, \quad \kappa_{pc} = 3.54 \times 10^{-13}\,\text{mm}^2,\\
&\kappa_e = 2.0 \times 10^{-11}\,\text{mm}^2.
\end{aligned}$$

The baseline values for the fluid parameters are summarized in Table 1.

Symbol	Unit	Meaning	Value	Reference
D	mm^2/s	Free diffusion coefficient	$D_{\text{free}}^{^{14}\text{C-inulin}} = 2.98 \times 10^{-4}$	[40]
D^*	mm^2/s	Apparent diffusion coefficient	$D^{*,^{14}\text{C-inulin}} = 1.03 \times 10^{-4}$	[40]
κ_j	mm^2	Permeability	$\kappa_a = 3.30 \times 10^{-6}, \kappa_v = 6.59 \times 10^{-6}, \kappa_c = 1.14 \times 10^{-9},$ $\kappa_{pa} = 1.0 \times 10^{-11}, \kappa_{pv} = 6.51 \times 10^{-9}, \quad \kappa_{pc} = 3.54 \times 10^{-13}, \kappa_e = 2.0 \times 10^{-11}$	[29] and computed
ϕ_j	No unit	Porosity	$\phi_e = 0.14, \phi_a = 0.00658, \phi_c = 0.00329, \phi_v = 0.02303$ $\phi_{pa} = 0.0006, \phi_{pc} = 0.0003, \phi_{pv} = 0.0021$	[15, 58, 41] and computed
μ_j	Pa s	Viscosity	$\mu_{pa} = \mu_{pv} = \mu_{pc} = \mu_e = 7.0 \times 10^{-4}$ $\mu_a = \mu_v = 2.67 \times 10^{-3}$	[12] [74]

Table 1: Baseline fluids (Blood and CSF) viscosity, permeability, porosity and diffusion parameters.

Exchange coefficients We first start by the exchange coefficients from blood to tissue, *i.e.* $\gamma_{e,a}, \gamma_{e,c}, \gamma_{e,v}$.

For these latter, we use the definition

$$\gamma_{j,i} = L_{i,j} \frac{|S_{i,j}|}{|\Omega|}.$$

As in [66], we use the hydraulic conductivities reported in [25, 37, 63]. We thus use the following values

$$L_{a,e} = 9.1 \times 10^{-10}\,\mathrm{mm/(sPa)}, \quad L_{c,e} = 1.0 \times 10^{-10}\,\mathrm{mm/(s\,Pa)}, \quad L_{v,e} = 2.0 \times 10^{-11}\,\mathrm{mm/(s\,Pa)}.$$

Furthermore, from [70], we estimate the ratio between surface area of capillaries and brain volume to

$$\frac{|S_{c,e}|}{|\Omega|} = 9\,\mathrm{mm}^{-1}.$$

Using the computations performed in [18], we assume that the surface density of capillaries is 3 times greater than the surface density of arteries and veins, *i.e.*

$$\frac{|S_{a,e}|}{|\Omega|} = 3\,\mathrm{mm}^{-1}, \quad \frac{|S_{v,e}|}{|\Omega|} = 3\,\mathrm{mm}^{-1}.$$

Altogether, we obtain

$$\gamma_{e,a} = 2.7 \times 10^{-9}\,(\mathrm{s\,Pa})^{-1}, \quad \gamma_{e,c} = 9.0 \times 10^{-10}\,(\mathrm{s\,Pa})^{-1}, \quad \gamma_{e,v} = 6.0 \times 10^{-11}\,(\mathrm{s\,Pa})^{-1}.$$

Then, we turn to the values of the exchange parameters from PVSs to ECS, *i.e.* $\gamma_{e,pa}, \gamma_{e,pc}, \gamma_{e,pv}$. From the 1D resistance parameters in [77], we compute the following coefficients (see Appendix A for details about the computations)

$$\gamma_{e,pa} = 2.2 \times 10^{-7}\,(\mathrm{s\,Pa})^{-1}, \quad \gamma_{e,pc} = 1.0 \times 10^{-9}\,(\mathrm{s\,Pa})^{-1}, \quad \gamma_{e,pv} = 2.0 \times 10^{-7}\,(\mathrm{s\,Pa})^{-1}.$$

From the previous values, we determine the following exchange coefficients for the transfer between blood vessels and PVSs (see Appendix A for details)

$$\gamma_{pa,a} = 2.76 \times 10^{-9}\,(\mathrm{s\,Pa})^{-1}, \quad \gamma_{pc,c} = 9.2 \times 10^{-9}\,(\mathrm{s\,Pa})^{-1}, \quad \gamma_{pv,v} = 6.0 \times 10^{-11}\,(\mathrm{s\,Pa})^{-1}.$$

For the exchanges between compartments corresponding to branching of blood vessel, we use

$$\gamma_{c,a} = \frac{B_{\mathrm{flow}}}{\Delta p_{c,a}\,|\Omega|} = 3.3 \times 10^{-6}\,(\mathrm{s\,Pa})^{-1}, \quad \gamma_{v,c} = \frac{B_{\mathrm{flow}}}{\Delta p_{v,c}\,|\Omega|} = 1.0 \times 10^{-5}\,(\mathrm{s\,Pa})^{-1}.$$

where $B_{\mathrm{flow}} = 2.4\,\mathrm{mL/min}$ (from [49]), and $\Delta p_{v,c}$ corresponds to the blood pressure drop between vessels. We assume a $\Delta p_{c,a} = 40\,\mathrm{mmHg}$ blood pressure drop from arteries to capillaries and a $\Delta p_{v,c} = 13\,\mathrm{mmHg}$ blood pressure drop from capillaries to veins.

To compute the exchange coefficients between the pial surface artery PVSs and the arterial PVS as well as for the exchange between ECS and SAS, we adapt the fluid resistance coefficient for this space from the one used in [77] to obtain (see Appendix A)

$$L_{\mathrm{PVSpial},pa} = 1.25 \times 10^{-6}\,(\mathrm{s\,Pa})^{-1}, \text{ and } Le, SAS = 3.13 \times 10^{-7}\,(\mathrm{s\,Pa})^{-1}.$$

The osmotic pressure in the capillary compartment has been reported to be 20 mmHg [36]. We thus set $\pi_a = \pi_c = \pi_v = 20\,\mathrm{mmHg}$ and $\pi_e = \pi_{pa} = \pi_{pc} = \pi_{pv} = 0.2 \times \pi_c$ (extravascular osmotic pressures have been chosen from the fact that due to the BBB the osmotic pressure in the ECS within the brain is known to be lower than 30% of the capillary one [36]).

We now define the advective mass exchange coefficients using the equation

$$\tilde{\gamma}_{j,i}^{^{14}\text{C-inulin}} = \gamma_{j,i}(1 - \sigma_{\mathrm{ij,reflect}}^{^{14}\text{C-inulin}}),$$

where $\sigma_{\text{ij,reflect}}^{^{14}\text{C-inulin}}$ is the reflection coefficient for the molecule and the membrane under consideration. Since Inulin is approximately 5000 Da in size (measured in [73]), we set

$$\sigma_{\text{ij,reflect}}^{^{14}\text{C-inulin}} = 0.2,$$

for all the membranes.

The diffusive permeabilities through the astrocyte endfeet (AEF) membrane for ^{14}C-inulin test case 2 and 3, are computed from [43, 48] (see Appendix A for details)

$$P_{pa,e}^{^{14}\text{C-inulin}} = P_{pv,e}^{^{14}\text{C-inulin}} = 1.25 \times 10^{-5}\,\text{mm}\,\text{s}^{-1}, \quad P_{pc,e}^{^{14}\text{C-inulin}} = 1.91 \times 10^{-6}\,\text{mm}\,\text{s}^{-1}.$$

From the two previous parameters, we defined for the 7 compartments system $\gamma_{pa,a}$, $\gamma_{pc,c}$, $\gamma_{pv,v}$, $\gamma_{e,pa}$, $\gamma_{e,pc}$, $\gamma_{e,pv}$ and $\gamma_{e,v}$ as well as their corresponding transfer coefficients for the two molecules.

The transfer of solutes between vessel compartments for which the connection exists without a membrane is assumed to be solely driven by convection and the fact that ^{14}C-inulin does not cross the BBB implies

$$P_{a,pa}^{^{14}\text{C-inulin}} = P_{v,pv}^{^{14}\text{C-inulin}} = P_{c,pc}^{^{14}\text{C-inulin}} = P_{a,c}^{^{14}\text{C-inulin}} = P_{c,v}^{^{14}\text{C-inulin}} = P_{pa,pc}^{^{14}\text{C-inulin}} = P_{pc,pv}^{^{14}\text{C-inulin}} = 0,$$

and for vessels in communications, the solvent-drag reflection coefficient is assumed to be $\sigma_{\text{reflect}} = 1$.

Altogether, we obtain the transfer coefficients reported in Table 2.

Symbol	Unit	Meaning	Value	Reference
$\gamma_{i\to j}$	1/(Pa s)	Fluid mass transfer coefficient	$\gamma_{a,e} = 5.73 \times 10^{-9}, \gamma_{v,e} = 1.26 \times 10^{-10}, \gamma_{c,e} = 1.9 \times 10^{-15}$ $\gamma_{pa,e} = 2.19 \times 10^{-7}, \gamma_{pv,e} = 1.95 \times 10^{-7}, \gamma_{pc,e} = 9.98 \times 10^{-10}$ $\gamma_{a,pa} = 5.89 \times 10^{-9}, \gamma_{v,pv} = 1.26 \times 10^{-10}, \gamma_{c,pc} = 1.9 \times 10^{-15}$ $\gamma_{a,c} = 1.05 \times 10^{-7}, \gamma_{c,v} = 5.25 \times 10^{-7}$ $\gamma_{pa,pc} = 2.50 \times 10^{-8}, \quad \gamma_{c,v} = 1.00 \times 10^{-7}$ $\gamma_{\text{PVSpial},pa} = 1.10 \times 10^{-5}, \gamma_{ECS,SAS} = 1.10 \times 10^{-7}$	Computed
$\tilde{\gamma}_{i\to j}^{^{14}\text{C-inulin}}$	1/(Pa s)	Advective mass transfer coefficient	Given by Eq. (21)	
$\lambda_{i\to j}$	s^{-1}	Solute mass transfer coefficient	$\lambda_{pa,e}^{^{14}\text{C-inulin}} = 3.74 \times 10^{-5}, \lambda_{pv,e}^{^{14}\text{C-inulin}} = 3.74 \times 10^{-5}, \lambda_{pc,e}^{^{14}\text{C-inulin}} = 1.71 \times 10^{-5}$	Computed from [42]

Table 2: Baseline diffusive and convective exchange parameters.

The last value we specify is the CSF volume surrounding the brain, *i.e.* in the subarachnoid space. This parameter value is required to define the boundary conditions. The reported values for this volume vary in the literature, ranging from 90 μL [56] to 520 μL [39], but seem to be consistently in the region 5-20% of the total intracranial volume. For the simulations in this paper we will assume that the CSF volume is 10.8% of the total intracranial volume, as reported by [50]. Assuming that the intracranial volume consist of brain tissue and the CSF spaces, then this value corresponds to a CSF volume of $V_{\text{CSF}} = 0.12 \times |\Omega|$, where $|\Omega|$ is the volume of the brain tissue.

Remark 3. *In the previous section, all the parameter values required to model the clearance of ^{14}C-inulin using Equation (1) or System (2) have been precised. Coefficients for which no value has been specified are assumed to be zero. This is the case for example for exchange coefficients between compartments that are not in communication.*

Remark 4. *Most of the parameter values have been found using measurements from in-vitro or in-vivo biological experiments. However, we have indicated the ones for which the values are adapted from the literature or the works from which we extracted the values estimated these parameters using numerical simulations. We recall that Appendix A provides details about the estimates and computed coefficients.*

2.4 Model variations

The effect of CSF clearance It has been suggested that flow of CSF in the SAS plays a major role for clearance also from the brain parenchyma [59, 30]. In the present study, the effect of CSF clearance from the SAS is modeled by three different boundary conditions for the concentration: 1) A homogeneous Dirichlet condition as described by Equation (2.2), representing instantaneous clearance from the SAS, 2) CSF/ISF exchange and conservation of tracer molecules in the intracranial compartment (Equation (12)), and 3) CSF/ISF exchange and exponential decay of particles from the SAS due to CSF production and absorption (Equation (11)).

The effect of sleep Xie *et al.* [80] reported an increase of the ECS porosity when the animal is sleeping. Indeed, they indicated that the porosity of the ECS in the awake state is $\phi_e^{\text{awake}} = 0.14$ whereas in the sleeping state they measured $\phi_e^{\text{sleep}} = 0.23$. Using the Kozeny-Carman equation this leads to the relation (see [72] for example)

$$\kappa_e^{\text{sleep}} = 5.5 \times \kappa_e^{\text{awake}}.$$

Recent results [13] indicate that when the animal is asleep, dilation and reduction of the perivascular spaces are observed due to vasomotion. Assuming that the vasomotion leads on average to an enhancement of PVS porosities and that the contraction of the blood vessels leads to a constant factor C_ϕ of increase of porosity for these spaces *i.e.*

$$\phi_j^{\text{sleep}} = C_\phi \phi_j^{\text{awake}}.$$

Then, assuming free (Poiseuille) fluid flow in perivascular spaces, a change of porosity creates a modification of the permeability leading to

$$\kappa_j^{\text{sleep}} = C_\phi^2 \kappa_j^{\text{awake}},$$

(see Appendix A for details). We assume that the parameter values corresponding to the awake state are given by the baseline values of Table 1. Based on the measurements from [13], we use an upper estimate of PVS variations during sleep, and assume $C_\phi = 4$.

The effect of communication with blood The blood vessels composing the cerebral vasculature are not completely impermeable, and there is debate going on to which extend CSF/ISF communicates with the microcirculation [54]. We consider both a 4-compartment model (test case 2) that assumes no communication between CSF/ISF and blood, and additionally a 7-compartment model (test case 3) where fluid can exchange between the blood vessels and the perivascular spaces around them.

2.5 Quantities of interest

To study the clearance of ^{14}C-inulin , we integrate the concentration for different volumes. To study how sample size variations from experimental data could affect the results, we integrate the concentrations over several cubes ω of varying sizes embedded in the brain mesh to represent possible measurement samples of the brain. In addition we assess the mass of molecules in the entire brain Ω.

For the first test case (ECS only), the relative mass of molecules in the entire brain at time t is denoted by

$$c_{tot}(t) := \frac{\int_\Omega \phi_e c_e(t, \mathbf{x}) \, \mathrm{d}\mathbf{x}}{\int_\Omega \phi_e c_e(0, \mathbf{x}) \, \mathrm{d}\mathbf{x}}.$$

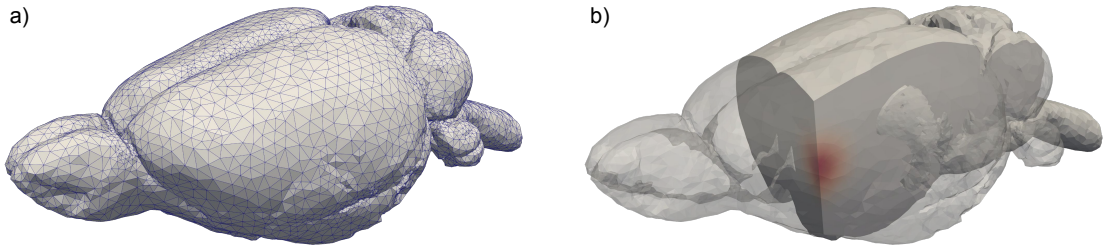

Figure 2: a): The computational mesh of the rat brain used for most of the simulations within this article. The meshing procedure is described in section 2.6. For the given mesh, the maximum cell size is $\approx 1/32$ times the diameter of the mesh. b): The initial ^{14}C-inulin concentration within the in the ECS, simulating an injection directly into the brain tissue.

The relative mass of molecule in the ECS within a cube $\omega \subset \Omega$ centered around the injection point is indicated by

$$c_\omega(t) := \frac{\int_\omega \phi_e c_e(t, \mathbf{x}) \, \mathrm{d}\mathbf{x}}{\int_\omega \phi_e c_e(0, \mathbf{x}) \, \mathrm{d}\mathbf{x}}.$$

For the other test cases (4, and 7-compartments), the relative mass of molecules in the entire brain and within a cube $\omega \subset \Omega$ at time t is denoted by

$$c_{tot}(t) := \frac{\int_\Omega \sum_{j \in J} \phi_j c_j(t, \mathbf{x}) \, \mathrm{d}\mathbf{x}}{\int_\Omega \phi_e c_e(0, \mathbf{x}) \, \mathrm{d}\mathbf{x}}, \quad c_\omega(t) := \frac{\int_\omega \sum_{j \in J} \phi_j c_j(t, \mathbf{x}) \, \mathrm{d}\mathbf{x}}{\int_\omega \phi_e c_e(0, \mathbf{x}) \, \mathrm{d}\mathbf{x}},$$

respectively.

We further measure the fluid velocity in the different compartments. From the solution of the pressure equations, we compute the vector fields

$$\mathbf{u}_j = -\frac{\kappa_j}{\phi_j \mu_j} \nabla p_j, \quad j \in J, \tag{14}$$

to obtain the velocity inside the j-th compartment. From these computed velocity fields, we compute the average velocity within a compartment $u_{\mathrm{aver},j}$ and the maximal velocity $u_{\mathrm{max},j}$ given by

$$u_{\mathrm{aver},j} = \frac{\int_\Omega |\mathbf{u}_j| \, \mathrm{d}\mathbf{x}}{|\Omega|} \quad u_{\mathrm{max},j} = \|\mathbf{u}_j\|_{L^\infty}, \tag{15}$$

To compute the volume of fluid transferring between compartment j and compartment i, we use

$$Q_{j,i} = \int_\Omega \gamma_{j,i} \, (p_i - p_j) \, \mathrm{d}\mathbf{x}. \tag{16}$$

To compute the volume of CSF exchanged between the compartment j and the SAS, we use

$$Q_{j,\mathrm{SAS}} = \int_{\partial\Omega} \left(-\frac{\kappa_j}{\mu_j} \nabla p_j \cdot \boldsymbol{\nu} \right) \mathrm{d}s. \tag{17}$$

To compute the mass of molecules moving from compartment i to j, we use [33]:

$$M_{ji}(t) = \int_\Omega \lambda_{j,i}(c_i - c_j) + \frac{(c_j + c_i)}{2} \tilde{\gamma}_{j,i}(p_i - p_j - \sigma_{i,j}(\pi_i - \pi_j)) \, \mathrm{d}\mathbf{x}. \tag{18}$$

2.6 Computational mesh, solution method and verification

The computational mesh used for the simulations in this paper was constructed from the "Waxholm Space Atlas of the Sprague Dawley Rat Brain v4" (RRID: SCR_017124) [55, 38], available under the licence CC-BY-SA 4.0 (https://creativecommons.org/licenses/by-sa/4.0/) at the following link: https://www.nitrc.org/projects/whs-sd-atlas. The atlas provides a detailed segmentation of different regions within the rat brain.

Since the models in this paper do not separate between tissue from different regions of the brain, we are mainly interested in the segments representing the ventricles, which are removed from the final mesh. The ventricle segments in the raw data file have a few irregularities. For example, in regions where the lateral ventricles are very thin, small groups of unlabeled voxels create holes in the 3D-reconstruction of the ventricles. To repair these irregularities we have made use of **3D Slicer**[1], an open-source software application for visualization and analysis of medical images [24]. 3D Slicer provides a segment editor with tools for manual labeling of voxels, hole filling and surface smoothing. After refining the segmentation of the ventricular system, it may be removed from the original volume, to create a realistic representation of the brain surface. The surface is exported as an `stl`-file to be used in the meshing algorithm.

The creation of the computational mesh is performed by SVMTK[2], which provides a python API for 3D mesh generation methods from the CGAL library. The mesh generation algorithm consists of a Delaunay refinement process followed by an optimization phase [2]. Following the procedures described in [46], we created the mesh illustrated in Fig 2a.

To solve the equations (1) and (2) we use the finite element method for the discretization in space and an implicit Euler method to integrate the resulting ordinary differential systems in time.

In this paper, we choose a resolution for the spatial mesh of $h = 1/32$. The temporal domain is $[0, T]$ with $T = 360\,\text{min}$ with a time step $\Delta t = 1\,\text{min}$. Details of the mesh and time resolutions can be found in Appendix B. The numerical scheme has been implemented using the FEniCS Library [3, 45], and the linear system was solved using the generalized minimal residual method (GMRES) and the incomplete LU (ILU) preconditioner. Our code is publicly available on GitHub at the following link: https://github.com/jorgenriseth/multicompartment-solute-transport.

3 Results

3.1 CSF flow in the 4-compartment model

Fig 3 depicts the pressure fields inside the different compartments for the 4-compartment model. We observe that for baseline parameter values, the pressure gradients in the different fields give a bulk flow of fluid in line with the glympathic theory. Indeed, using Equation (14), our model represents an inflow of CSF from the surface of the brain in the PVS of arteries and an outflow from the PVS of veins. Smaller pressure gradients leading to lower velocities directed from the surface to the depth of the brain are also seen in the ECS and the PVS of capillaries.

Computing the transfer of CSF between the compartments using Equation (16), we obtain

$$Q_{pa,e} = 0.91\,\mu\text{L/min}, \quad Q_{e,pv} = 0.33\,\mu\text{L/min}, \quad Q_{e,pc} = 0.52 \times 10^{-3}\,\mu\text{L/min}.$$

[1] https://www.slicer.org/
[2] https://github.com/SVMTK/SVMTK

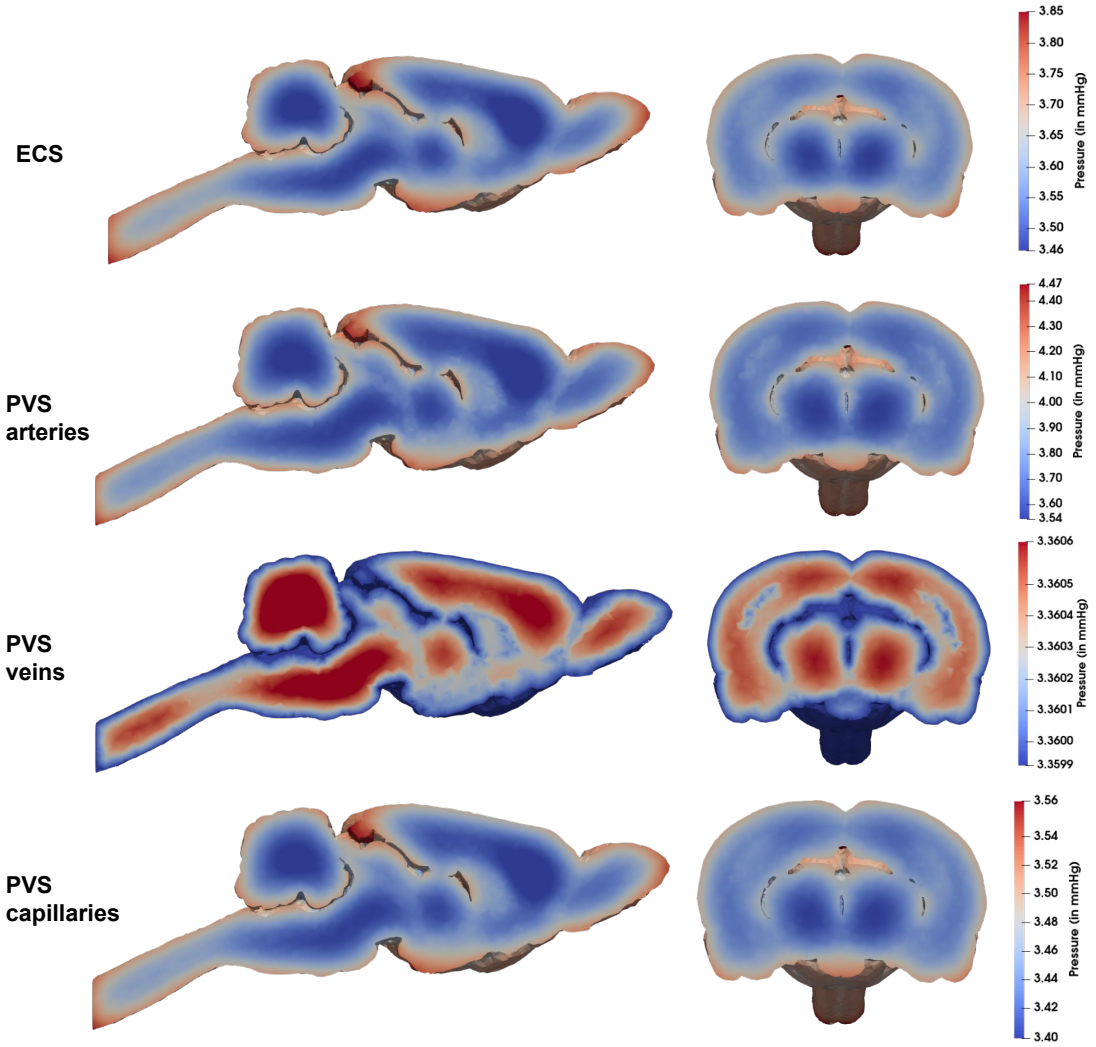

Figure 3: Pressure fields in the 4 compartments (left: coronal cut, right: sagittal cut)

Compartment	u_{aver} (in μm/s)	$u_{\max}$ (in μm/s)
PVS arteries	2.8	27
ECS	4.9×10^{-3}	7.3×10^{-2}
PVS veins	0.74	5.2
PVS capillaries	3.4×10^{-2}	0.18

Table 3: Velocities of CSF in the different compartments.

The transfer between the compartments and the SAS is computed in the same way using Equation (17), and we obtain

$$Q_{\text{SAS},e} = 0.36\,\mu\text{L/min}, \quad Q_{\text{SAS},pa} = 0.72\,\mu\text{L/min}, \quad Q_{pv,\text{SAS}} = 0.37\,\mu\text{L/min}.$$

In this notation, we choose subscripts such that the flow occurs from the first denoted compartment to the second (e.g. flow occurs from the PVS of arteries to the ECS).

From these pressure fields, we compute the velocity of the CSF in the compartments using Equation (14). We report the average velocities u_{aver} and the maximal ones $u_{\max}$ for each compartment in Table 3

3.2 Transport within the brain

In the following two subsections, we report the relative amount of ^{14}C-inulin in the entire brain from the diffusion and the 4-compartment simulations using Equation (9) with (11) as boundary conditions. We then vary the size of the measurement sample (*i.e.* the domain in which the remaining mass of ^{14}C-inulin is computed) and the boundary conditions.

3.2.1 Diffusion in the ECS only

Pure diffusion steadily decreased the amount of tracers found within the brain over the entire simulation time and ∼53% of the tracer remains after 6 hours (Fig 4a, blue dashed line). Fig 4c shows the distribution of ^{14}C-inulin transported by pure diffusion (*i.e.* Equation (1)) in the ECS at different points in time. The tracer spreads radially out from the point of injection, and peak concentration has decreased drastically after T = 360 min. At the first time step, some very small negative values appear near the tail of the Gaussian curve, but are smoothed out over time.

3.2.2 4-compartment convection-diffusion

Fig 5 shows the spatial distribution of ^{14}C-inulin concentration over time in all 4 compartments considered in ^{14}C-inulin test case 2. Initially, the tracer is contained only in the ECS where it first was injected. Already after 10 minutes, the concentration spreads equally to all compartments. From all time points on, the tracer spreads radially outwards in all compartments, similar to the test case for pure diffusion. We note here that even with equal concentrations, the total mass of tracer differs between each compartment due to differences in porosity. ^{14}C-inulin is thus mainly still contained to the ECS in the 4-compartment model. The tracer in the 4-compartment convection-diffusion model is cleared from the brain slightly faster compared to diffusion alone and ∼49% of the tracer remains in the brain after 6 hours.

3.2.3 Effect of the measurement sample

Fig 4a shows the evolution of the relative mass of ^{14}C-inulin inside the rat brain and in samples of the brain of different sizes (cubes of side length 2mm, 4mm, and 5mm). The boundary

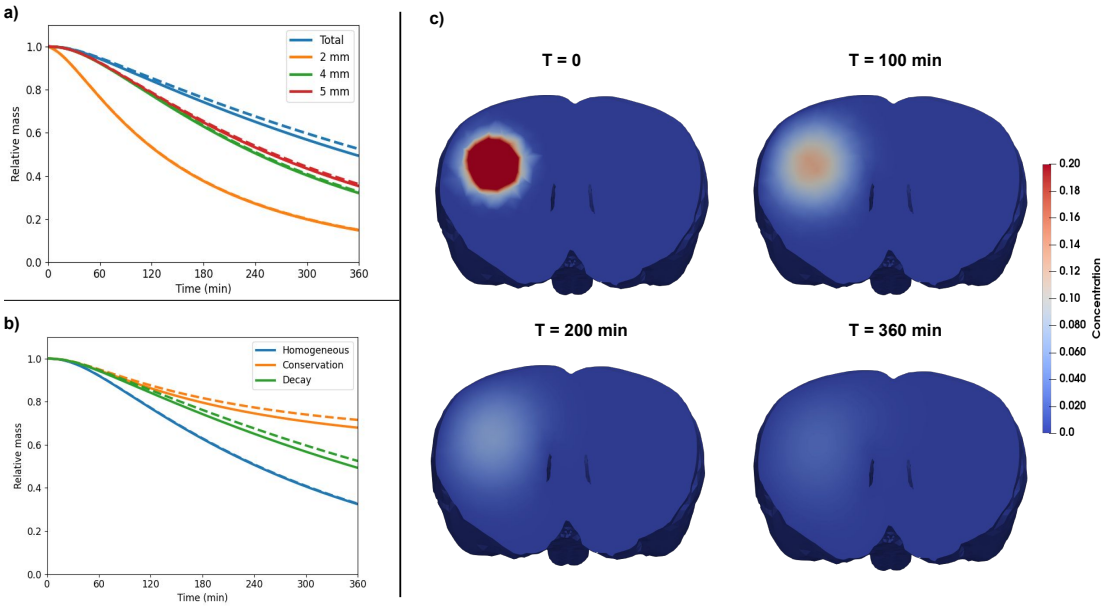

Figure 4: a) Relative ^{14}C-inulin mass located within regions of varying size surrounding the injection point. Solid lines result from the multi-compartment model simulations while dashed lines result from diffusion only in the ECS. b) Relative ^{14}C-inulin mass located in the totality of the brain for the different boundary conditions. Solid lines result from the multi-compartment model simulations while dashed lines result from diffusion only in the ECS. c) Evolution in space and time of ^{14}C-inulin relative concentration in the ECS for test case 1 (single diffusion). The color scale is chosen for a visual comparison between all time points.

conditions for the concentration equations correspond to the time dependent Dirichlet boundary conditions (11). For the smallest measurement sample, the relative mass of tracers remaining in the sample after 6 hours were ∼15% for diffusion and for the 4-compartment model (compared to 53% and 49% for the entire brain). In general, we observe that as the measurement sample size increases the mass of ^{14}C-inulin remaining in the sample increases.

3.2.4 Effect of the concentration in the subarachnoid space

Fig 4b shows the evolution of the relative mass of ^{14}C-inulin for the three different boundary conditions for the concentration equations: Homogeneous Dirichlet boundary condition, conservation of the mass in the subarachnoid space (corresponding to Equation (9) with (13)), and clearance of molecules in the subarachnoid space (corresponding to Equation (9) with (11)). Fig 4b compares the relative mass of tracer for the diffusion model (dashed lines) to the four-compartment model (solid lines). In both models, the homogeneous Dirichlet boundary conditions lead to fast clearance from the tissue with $\sim$ 33% remaining in the brain after 6 hours (For both diffusion only and the 4-compartment simulations). When the concentration of ^{14}C-inulin is computed using the time dependent Dirichlet boundary conditions representing tracer conservation in the SAS, the mass of tracers is close to plateau level at 68% or 72% at 6 hours. With the time dependent boundary conditions modelling absorption of CSF in SAS, the relative tracer mass steadily decreases, and ends up in between the two previously described cases with 49-53% of

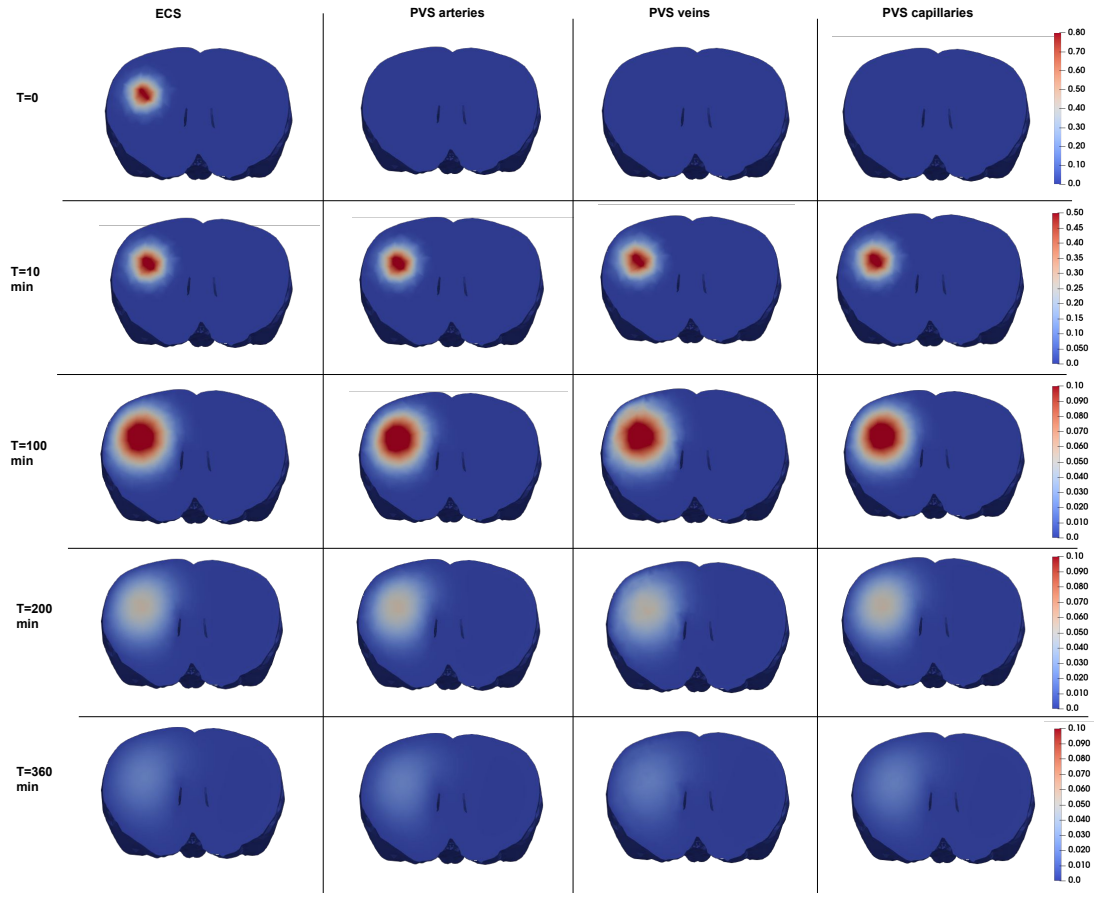

Figure 5: Evolution in time and space of the relative ^{14}C-inulin amount in the rat brain (frontal cut at the injection point) within the 4 compartments of test case 2.

the tracer remaining in the brain after 6 hours.

3.3 Variations of the 4-compartment model

3.3.1 Effect of an increase in ECS porosity

With an increase of ECS porosity from 0.14 to 0.23, we find no relevant difference for the total amount of CSF transferring between the compartments. Interestingly, we find that the maximum velocity in the ECS increases to $u_{\max} = 9.7 \times 10^{-2}\,\mu$m/s (from $7.3 \times 10^{-2}\,\mu$m/s) and the average velocity of CSF in ECS increases to $6.6 \times 10^{-3}\,\mu$m/s (from $4.9 \times 10^{-3}\,\mu$m/s). See Table 3 for all reference velocities computed with baseline parameter values.

Tracer clearance is slightly slower for the four-compartment model when ECS porosity is increased (blue versus orange line, Fig 6). As the velocity field in the ECS is directed from the surface of the brain towards the ventricles, additional flow in the ECS slows down clearance in this compartment, and the relative mass of tracers within the brain is in this case 56% after 6 hours.

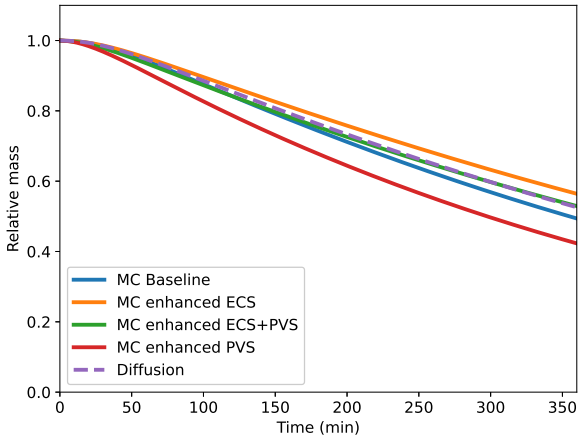

Figure 6: Comparison of ^{14}C-inulin clearance for different variations of porosity and permeability coefficients. "MC Baseline" denotes the clearance curve given by the multi-compartment model with baseline parameter values and is hidden by the dashed curve "Diffusion" representing the clearance given by the application of the Diffusion model in the ECS compartment only. The enhancement of ECS porosity leads to the curve denoted "MC enhancement ECS" and the increase of the porosities in all the compartments gives the clearance curve denoted "MC enhancement ECS+PVS"

3.3.2 Effect of an increase in PVS porosity

Increasing the PVS porosity by a factor 4, increases clearance from the brain via PVS. The relative mass of tracers found in the brain after 6 hours decreased from 53 % during baseline to 42% with increased PVS porosity (Figure 6, blue versus red line). Indeed, since the diffusive transfer between the compartments tends to average the concentration between them, increasing the porosity of PVSs increases the mass of ^{14}C-inulin in these compartments. Since the PVS of veins is larger than the other and is a outflow route (with a convective field directed to the surface of the brain) clearance of ^{14}C-inulin appears faster.

3.3.3 Combined enhancement of the extracellular volume and perivascular spaces

Combining the increase of both ECS and PVS porosity and permeability, we obtain the following computed amount of CSF transfer between the compartments

$$Q_{pa,e} = 2.2\,\mu\text{L/min}, \quad Q_{e,pv} = 1.0\,\mu\text{L/min}, \quad Q_{e,pc} = 2.4\times10^{-3}\,\mu\text{L/min},$$
$$Q_{e,\text{SAS}} = 1.0\,\mu\text{L/min}, \quad Q_{\text{SAS},pa} = 2.3\,\mu\text{L/min}, \quad Q_{pv,\text{SAS}} = 1.1\,\mu\text{L/min}.$$

We also obtain the maximum and averaged velocities reported in Table 4.

With an increase in both ECS and PVS permeability, we observe a very similar clearance compared to baseline values (Figure 6, blue versus green line). The clearance of ^{14}C-inulin is initially slightly faster with the enhanced porosity, however after 6 hours pure diffusion and the 4-compartment model reach both 53% of ^{14}C-inulin mass in this case.

Compartment	u_{aver} (in μm/s)	$u_{\max}$ (in μm/s)
PVS arteries	4.5	26
ECS	1.2×10^{-2}	0.15
PVS veins	0.97	6.4
PVS capillaries	4.2×10^{-2}	15×10^{-2}

Table 4: Velocities of CSF in the different compartments for an increase of porosity and permeability in all the 4 compartments.

3.4 7-compartment model: Additional effect of cerebral blood perfusion

Using the baseline parameter values for the second and the third test cases, we obtain the velocity fields in the PVS of arteries shown in Fig 7a. Interestingly, the leakage of fluid from arteries and capillaries to the PVSs occuring in the 7-compartment model, changes the pressure fields compared to the 4-compartment model (shown in Fig 3), in which the PVSs were assumed to be isolated from the blood. In contrast to the 4-compartment model, the fluid flow in the PVS of arteries and the ECS is directed towards the brain surface. In addition, flow velocities are increased compared to the 4-compartment model (see Table 5 for details).

Fig 7b shows the clearance curves of ^{14}C-inulin obtained with all three test cases (pure diffusion, 4-compartment, 7-compartment). We observe that with the additional effect of blood perfusion, the clearance is much faster compared to both pure diffusion and all variations of the 4-compartment model. Only $\sim 5\%$ of the tracer remains in the brain after 6 hours for the 7-compartment model (compared to 53% and 49% for pure diffusion and 4-compartment model).

Compartment	u_{aver} (in μm/s)	$u_{\max}$ (in μm/s)
Arterial blood	3.3×10^2	6.4×10^3
Venous blood	46	3.1×10^2
Capillary blood	4.2	1.4×10^2
PVS arteries	27	1.5×10^2
ECS	1.3×10^{-2}	6.8×10^{-2}
PVS veins	31	1.8×10^2
PVS capillaries	0.21	1.0

Table 5: Velocities of CSF and blood in the different compartments for baseline values coefficients for test case 3.

Computing the fluid flow between the different compartments using Equation (16), we find

$$\begin{aligned} Q_{a,pa} = 12\,\mu\text{L/min}, \quad Q_{v,pv} = 8.4 \times 10^{-3}\,\mu\text{L/min}, \quad Q_{c,pc} = 1.2\,\mu\text{L/min}, \\ Q_{pa,e} = 7.7\,\mu\text{L/min}, \quad Q_{e,pv} = 6.1\,\mu\text{L/min}, \quad Q_{e,pc} = 1.5 \times 10^{-2}\,\mu\text{L/min}, \\ Q_{a,\text{influx}} = 205\,\mu\text{L/min}, \quad Q_{v,\text{outflow}} = 145\,\mu\text{L/min}, \quad Q_e, \text{SAS} = 1.46\,\mu\text{L/min}, \\ Q_{\text{SAS},pa} = 1.2\,\mu\text{L/min}, \quad Q_{pv,\text{SAS}} = 6.2\,\mu\text{L/min}. \end{aligned}$$

4 Discussion

The main goal of this article is to propose a multi-compartment model representing the fluid movement and solute transport in the brain. We apply our model to the modelling of the

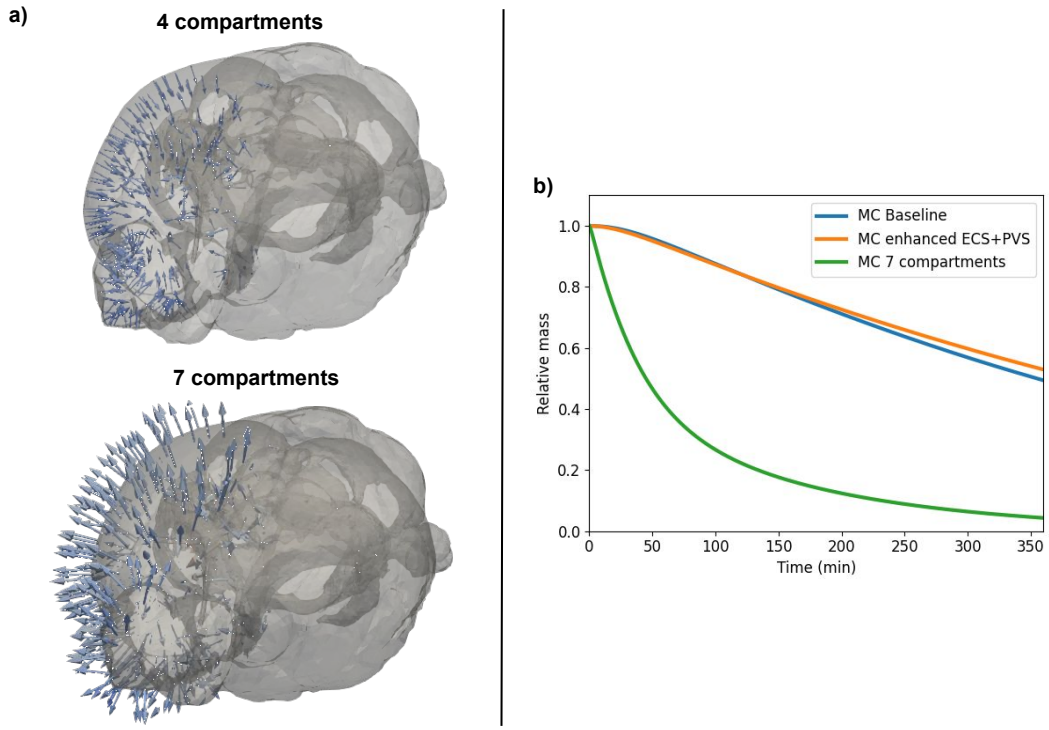

Figure 7: a) Comparison of velocity fields in PVS arteries for test case 2 and 3. The velocity field is oriented to the outside of the brain and the magnitude is larger when blood is considered in the model. b) Comparison of ^{14}C-inulin clearance for test case 2 with baseline parameter values and increase of ECS and PVSs porosities with test case 3. "MC Baseline" denotes the clearance curve given by the multi-compartment model with baseline parameter values. The enhancements of ECS and PVSs porosities lead to the curve denoted "MC enhancement ECS+PVS" and the result of test case 3 is denoted "MC 7-compartments"

glymphatic system at the scale of the rat brain. We design our model and numerical method to explore different scenarios and hypotheses related to clearance of molecules from the brain. Indeed, changing the parameter values for permeability, porosity, exchange coefficients allows to represent for example the possible effect of sleep, the disruption of a membrane, an enhanced CSF flow in the parenchyma or the effect of blood perfusion on the standard picture depicted by the Glymphatic theory. Furthermore, the numerical results explore different situations and allow to access the importance of different modelling aspects such as the boundary conditions but also biological experimental aspects such as the importance of the measurement sample. To best of the authors knowledge this is the first attempt of using a multi-compartment model to combine fluid flow and transport of solute at the scale of the entire brain. This work is largely built upon works related to blood perfusion in tissues [67, 68, 57].

Effect of the measurement sample The effect of the measurement sample is depicted in Fig 4a. Our results show that if the measurement sample is small, clearance appears to be faster compared to larger samples or the entire brain. This information needs to be taken into account when quantitatively comparing biological experiments to simulations (e.g. clearance curves). For instance, comparisons between simulation results and the results obtained by e.g. Iliff et al. [32] and measurements in a piece of tissue or slice (e.g. tracer influx in Xie et al. [80]) is not straightforward.

Modelling the clearance of ^{14}C-inulin from the SAS using boundary conditions Usually, mathematical models representing clearance of molecules from the brain use homogeneous Dirichlet boundary conditions for the concentrations (*e.g.* see [29, 71]). This modelling assumes that clearance in the SAS is instantaneous which is in reality not the case. Some studies have taken this into account by adding a mass conservation between the brain and the SAS [14]. However, the numerical results presented on Fig 4b show that taking the concentration of solutes in the CSF in the SAS into account leads much slower clearance rates (there are 39% less relative ^{14}C-inulin mass cleared assuming conservation of molecules in SAS than for homogeneous Dirichlet boundary conditions after 6 hours). Even when adding an absorption rate of CSF in SAS, we also obtain slower clearance rates compared to homogeneous Dirichlet boundary conditions (There is a difference of 20% of relative ^{14}C-inulin mass after 6 hours between the boundary conditions modelling slower clearance from the CSF in the SAS and the homogeneous boundary condition). Hence, our results indicate that forthcoming mathematical models should be careful with the choice of boundary conditions to obtain biologically relevant results.

Baseline parameter values for the multi-compartment model corresponds to the awake state Even though the model comprises a lot of parameters, most of them can be estimated using measurements reported in the literature. Using baseline parameter values, diffusion in the ECS (test case 1) gives clearance results very similar to the ones given by the 4-compartment model considering the PVSs as being isolated from the effect of blood perfusion (test case 2). The results from these models correspond qualitatively to the clearance results reported in Xie *et al.* [80] for the awake state. Therefore, these results indicate that the baseline parameter values correspond to the an animal in the awake state and that diffusion in the ECS is the main mechanism to explain the observed clearance. The latter point is explained by the much larger volume fraction of ECS compared to the PVSs. Most of the ^{14}C-inulin mass is thus contained and cleared within the ECS. Therefore, even though the Péclet number is higher in the PVSs than in the ECS (Pe $= 9.4$ in the PVS of arteries compared to Pe $= 1.6 \times 10^{-2}$ in the ECS), most of the transport still occurs in the latter.

Increasing the porosity of the ECS slows the clearance of ^{14}C-inulin Since the work of Xie *et al.* [80], sleep is believed to play an important role in the clearance of molecules. In [80], an increase of the porosity of the ECS was measured when the animal was asleep. Our results show that when only the ECS porosity was increased, the clearance of ^{14}C-inulin was slower. This may be explained by the fact that increasing the ECS porosity leads to smaller concentration gradients, hence decreasing diffusive movement. However, in this scenario, we assumed that the diffusion coefficient remained constant. Furthermore, the increased ECS porosity only led to a 74% increase in average velocity, and still the Péclet number remains small ($\mathrm{Pe} = 2.2 \times 10^{-2}$ after ECS porosity increase) in the ECS.

Compared to the usual representation of the glymphatic system in which vessels are clearly spaced and convective movement occurs between them, our multi-compartment model represents this effect through the exchange terms. The enhancement of the ECS porosity allows for more fluid transfer from the ECS to PVS veins (as shown in Subsection 3.3.3), hence, capturing well the hypothesized faster convective movement in the ECS from the PVS of arteries to the PVS of veins during sleep. However, the usual schematic representation of the glymphatic system does not allow to consider the directions of the pressure gradients in the ECS at the scale of the brain. If we assume that the convective movement in the PVS of arteries is generated by a pressure gradient, our results show fluid flow in the ECS directed inwards from the surface of the brain. This latter counters the diffusive movement and, hence, slows down the clearance of solutes. This could indicate an effect that is neglected in the current glymphatic theory and needs further investigations.

The minor effect of increased porosity in our model seems to indicate that to obtain the measured effect of sleep (see Xie *et al.* [80]), another induced change must take place. Recent results from [13] indicate that sleep also induces vasomotion in the brain. If we assume that sleep induces a general vasoconstriction trend, we can model this effect by reducing the radius of blood vessels, and hence, the PVS width increases. Therefore, porosity and permeability coefficients are adapted correspondingly (see Appendix A). This leads to an enhanced CSF movement in all structures (e.g. an increase of 350% of fluid volume from the PVS of arteries to the ECS) and affects the clearance of ^{14}C-inulin . The clearance curves shown in Fig 6 clearly reveal that the clearance is faster for the scenario in which PVS porosities are increased. Furthermore, it is worth mentioning to obtain similar results as the ones obtained in Xie *et al.* [80] for ^{14}C-inulin clearance for sleeping animals (45% clearance after 4 hours), we would need to increase only the porosity of the PVSs in an unrealistic way. Therefore, our results for the 4-compartment indicate that the improvement of clearance due to sleep does not seem to be explained only by an increase of the porosity coefficients in the ECS and PVSs.

Fluid leakage from the blood vessels improve ^{14}C-inulin clearance and make the peri-arterial space an outflow route Using biological relevant parameter values, our results indicate that if the effect of leakage from the blood vessels is taken into account, the flow of CSF in the PVS of arteries is reversed compared to the standard picture of the glymphatic theory. With inclusion of blood vessels, the flow direction is in line with the proposed hypothesis by Cserr et al. [16]. Hence, the PVS arteries compartment becomes an outflow route in this case as observed in Fig 7a. Additionally, the flow is also reversed in the ECS compared to the 4-compartment model. This leads to a faster clearance of ^{14}C-inulin as observed in Fig 7c. For this third test case the relative amount of ^{14}C-inulin decays exponentially with $\sim$5% of relative ^{14}C-inulin mass after 6 hours. The shape for the clearance curve corresponds more to the sleeping animals results from Xie *et al.* [80]. Therefore, combining our results from the 4- and 7-compartment models seem to indicate that the transfer of fluid between blood vessels and PVSs and ECS provide a great potential to increase clearance during sleep. This could be related again to observed

vasomotion of cerebral vessels during sleep [13].

Limitations and further works Our model is based on a homogenization procedure that represents the different structures (ECS, PVS, blood vessels) as a continuum. We know that porous media can be homogenized into a single continuous medium if the pores distance does not exceed a certain value. Usually, the derivation of the macroscopic model is assumed to be correct if the ratio between the length scale of the pores (in our case the distance between vessels) and the length scale of the chamber is less than one. In our model, this holds true for most compartments (see Shipley *et al.* [68] for homogenization related issues). However, we emphasize that this ratio is close to one for cerebral arterioles and venules. Therefore, our macroscopic continuous view of the glymphatic system and cerebral blood perfusion has to be viewed as a coarse approximation of the real phenomenon. This strong modelling assumption could be relaxed considering a 1D-3D model (see *e.g.* [17]) in which the ECS only is represented as a continuous medium while the other structures are modelled by 1D lines. This type of model can describe more accurately the glymphatic system and the cerebral vascular tree but is too costly to be used at the scale of the total brain. However, some of the observations and assumptions from this present work could be tested and verified more accurately with such a 1D-3D model. The comparison between these two types of models will be the subject of a future work.

In our article, the clearance of solutes from the CSF in the SAS is taken into account using a simplified boundary condition. Indeed, we assumed that once the solute reaches the SAS it diffuses instantaneously within the CSF in this region. We plan to derive more rigorously these boundary conditions in a future work by first modelling fluid movement inside a three dimensional subarachnoid space and then seeking effective boundary conditions while studying the asymptotic limit of zero width for the subarachnoid space.

Furthermore, due to the complexity induced by the modelling of the different compartments and exchange between them, there are 8 coefficients per compartment (some of them might be shared between two compartments, for example for the exchange through a shared membrane). Some measurements of these parameters exist, however sometimes in different species (rats versus humans), and we have to the best of our ability translated parameters to reflect rat physiology. In addition, the measured values may suffer from experimental uncertainties. This can be clearly seen if we take for the example the permeability of the ECS κ_e. We can find in the literature very different values for this coefficient as previously mentioned by Holter *et al.* [29]. This illustrates the uncertainty concerning the ECS permeability value on which many of the other permeabilities are based (see Appendix A). Furthermore, understanding the effect of small variations of all parameter values on the results is out of scope of the present study. Sensitivity analysis for some of the important parameters will be the subject of a forthcoming work.

In our study, we made some variations of parameter values to model possible increase of ECS or PVSs volumes. The enhancement of ECS volume is reported in [80]. However, the increase of PVSs volume has been measured recently in [13] and does not appear to be a fixed parameter but rather a time dependent value. Indeed, oscillations, vasoconstrictions and vasodilatations may occur over a few minutes (see Fig 2d in [13]). If the effect of these oscillations in porosity were accounted for in our model, the equations change drastically ($\phi(t)$ becomes a time dependent function and stays in the time derivative of both the concentration and pressure equations). Adding the effect in the system forces us to keep the time derivative in the pressure equation and solve at each time step a coupled system of equations for each compartment. This will increase tremendously the computational cost of the simulations.

The use of standard continuous finite elements for the discretization of the diffusion equation leads to the presence of small oscillations of the numerical solution. See e.g. [46] for details

about this effect and some remarks about stabilization, which could be included in further works. However, we note that integrated quantities over large domains (e.g. the brain) is not affected as small oscillations around zero concentration evens out. In this work we arranged the scale on the figures so that no negative values for the concentration appear.

Conclusion In this paper we presented a multi-compartment model for fluid and solute transport with application to the glymphatic system of a rat brain. The model allows us to test the effect of different physiological changes (e.g. sleep), and assess different theories concerning fluid flow and transport in the brain. Unless blood filtration was added to the model, diffusion was the main driving force for transport. However, as our simulations show, only a small leakage from blood vessels increased clearance by an order of magnitude.

A Computing biologically relevant parameters

A.1 Permeability coefficients

In the present article we mostly use another definition that can be obtained from the resistance values given in [77]. Even though this work deals with a one dimensional model, a relation between these 1D resistances to 3D permeabilities can be found. Indeed, assuming that we have any 1D line embedded into a 3D cylinder of length L and cross sectional area A, the volumetric flux in the 1D geometry is given by Poiseuille equation

$$Q = \frac{1}{R}\Delta p,$$

where R is the resistance in the 1D geometry and Δp is the pressure difference between the two ends of the line. Then, if we assume that the flow in the 3D cylinder is given only by the flow in the line, Darcy's law gives the relation

$$Q = \frac{\kappa}{\mu}\frac{A}{L}\Delta p = \frac{1}{R}\Delta p,$$

where κ is the averaged permeability and μ is the dynamic viscosity. Altogether, we obtain

$$\kappa = \frac{\mu L}{RA}. \tag{19}$$

The coefficient $\frac{L}{A}$ is arbitrary because it depends on the choice of cylinder for the homogenization step. Therefore, knowing the permeability of the ECS for example from [29], is enough to find the value of this coefficient and gives a direct relation between R_j and κ_j. These resistance coefficients R for the different compartments can be found in [77]. Choosing a permeability for the ECS of $\kappa_e = 2.0 \times 10^{-11}\,\mathrm{mm}^2$, a CSF dynamic viscosity of $\mu_e = 0.7 \times 10^{-3}\,\mathrm{Pa\,s}$, and the resistance coefficient $R_e = 4.56(\mathrm{Pa\,s})/\mathrm{mm}^3$ indicated in [77] we have

$$\frac{L}{A} = 1.1 \times 10^{-7}\,\mathrm{mm}^{-1},$$

and we obtain the values for the permeability coefficients

$$\kappa_{pa} = 1.0 \times 10^{-11}\,\mathrm{mm}^2, \kappa_{pv} = 6.51 \times 10^{-9}\,\mathrm{mm}^2, \kappa_{pc} = 3.54 \times 10^{-13}\,\mathrm{mm}^2.$$

Then, from [20] and [35]

$$\kappa_a = 3.30 \times 10^{-6}\,\mathrm{mm}^2, \kappa_v = 6.59 \times 10^{-6}\,\mathrm{mm}^2, \kappa_c = 1.14 \times 10^{-9\,\mathrm{mm}^2}.$$

However, in previous works, authors evaluated these coefficients through numerical testings, leading to very different values. Indeed, from [74, 26, 21] in which the MPET equations are used to represent the movement of CSF through different compartments, permeabilities are

$$\kappa_a = \kappa_v = \kappa_c = \kappa_{pa} = \kappa_{pv} = \kappa_{pc} = 1.0 \times 10^{-4}\,\mathrm{mm}^2, \text{ and } \kappa_e = 1.4 \times 10^{-8}\,\mathrm{mm}^2.$$

Therefore, we obtain a difference between these two parameter sets of several order of magnitude, leading to tremendous differences in fluid movement.

A.2 Transfer coefficients

Following Starling equation, the definition of the coefficients is for transfer between vessels and tissues

$$\gamma_{i,j} = L_{i,j}\frac{|S_{i,j}|}{|\Omega|}, \tag{20}$$

where L_{ij} is the hydraulic conductivity of the membrane (in $\mathrm{mm}/(\mathrm{s\,Pa})$), $\frac{|S_{ij}|}{|\Omega|}$ is the ratio between the surface area of the vessel per unit of volume of tissue (in mm^{-1}).

We know the ratio $\frac{|S_{i,j}|}{|\Omega|}$, but we are missing the value of the hydraulic conductivity for some of the considered membranes. For the transfer from blood vessels to ECS, we can find the value of the hydraulic conductivity of the BBB at the different levels (*i.e.* arteries, capillaries and veins). The values are reported in the main body of this article, in Section 2.

For the transfer coefficients between PVSs and the ECS, we use the following method. We search a suitable relation between the 1D resistance parameters from [77] and the 3D exchange coefficients $\gamma_{j,i}$. In the following we assume that the transfer coefficients for the PVSs to ECS are comparable between human to rat.

Starting from the volumetric flow $Q_{j,i}$ through a 1D structure

$$Q_{j,i} = \frac{1}{R_{j,i}}(p_i - p_j),$$

where $R_{j,i}$ is the resistance through the structure and using the fact that this same volumetric flux in 3D is given by

$$Q_{j,i} = \int_\Omega \gamma_{j,i}(p_i - p_j)\,\mathrm{d}x,$$

assuming that the pressure difference $(p_i - p_j)(x)$ is constant in space (which is not unreasonable since the transfer coefficient is homogeneous in space as well), we obtain the relation

$$\gamma_{j,i} = \frac{1}{R_{j,i}\,|\Omega|}.$$

We emphasize that since the resistance coefficients reported here are for human, the volume $|\Omega|$ is the volume of the human brain, *i.e.* $|\Omega| = 1 \times 10^{-6}\,\mathrm{mm}^3$. Thus, from this equation we can define the transfer coefficient in a different manner using only the 1D resistances estimated in [77] and the volume of our computational domain.

We apply the previously presented method to compute the exchange coefficients between PVSs and ECS. We obtain

$$\gamma_{pa,e} = 2.19 \times 10^{-7}\,(\mathrm{Pa\,s})^{-1}, \gamma_{pv,e} = 1.95 \times 10^{-7}\,(\mathrm{Pa\,s})^{-1}, \gamma_{pc,e} = 9.98 \times 10^{-10}\,(\mathrm{Pa\,s})^{-1}.$$

For the exchange from blood vessels to ECS, we obtain

$$\gamma_{a,e} = 5.73 \times 10^{-9}\,(\mathrm{Pa\,s})^{-1}, \quad \gamma_{v,e} = 1.26 \times 10^{-10}\,(\mathrm{Pa\,s})^{-1}, \quad \gamma_{c,e} = 1.26 \times 10^{-9}\,(\mathrm{Pa\,s})^{-1}.$$

To compute the fluid exchange coefficients between blood vessels and PVSs, we compute the resistance of the blood brain barrier at the different levels (*i.e.* arteries, veins, capillaries) and subtract to it the resistance of the astrocyte end-feet barrier. We obtain the relation

$$R_{a,pa} = \frac{1}{\gamma_{e\leftarrow a}\,|\Omega|} - R_{pa,e}, \quad R_{a,pv} = \frac{1}{\gamma_{e\leftarrow v}\,|\Omega|} - R_{pv,e}.$$

Knowing these resistances and using the previous method, we can compute the coefficients

$$\gamma_{a,pa} = 5.89 \times 10^{-9}\,(\mathrm{Pa\,s})^{-1}, \quad \gamma_{v,pv} = 1.26 \times 10^{-10}\,(\mathrm{Pa\,s})^{-1}.$$

For the capillary level, we use the method from [66] to obtain the resistance of the BBB membrane in which we suppressed the AEF membrane. We obtain

$$\gamma_{c,pc} = 2.98 \times 10^{-9}\,(\mathrm{Pa\,s})^{-1}.$$

Next, we need to specify the transfer coefficients for connected spaces, *e.g.* from arteries to capillaries. To do so, we use the equation

$$\gamma_{j,i} = \frac{Q}{|\Delta p_{i,j}|},$$

where Q is the flow rate of fluid (CSF or blood) and $\Delta p_{i,j}$ denotes the pressure drop from one compartment to the other. Using a cerebral blood flow of $Q_{\mathrm{blood}} = 700\,\mathrm{mm}^3/\mathrm{s}$, a pressure drop from arteries to capillaries of $\Delta p_{a,c} = 50\,\mathrm{mmHg}$, and a pressure drop from capillaries to veins of $\Delta p_{a,c} = 10\,\mathrm{mmHg}$, we obtain

$$\gamma_{a,c} = 1.05 \times 10^{-7}\,(\mathrm{Pa\,s})^{-1}, \quad \gamma_{c,v} = 5.25 \times 10^{-7}\,(\mathrm{Pa\,s})^{-1}.$$

Then, assuming a total flow rate of CSF through perivascular spaces of $Q_{\mathrm{CSF}} = 3.33\,\mathrm{mm}^3/\mathrm{s}$, and a pressure drop from PVS arteries to PVS capillaries of $\Delta p_{pa,pc} = 1\,\mathrm{mmHg}$, and a pressure drop from PVS capillaries to PVS veins of $\Delta p_{pa,pc} = 0.25\,\mathrm{mmHg}$, we obtain

$$\gamma_{pa,pc} = 2.50 \times 10^{-8}\,(\mathrm{Pa\,s})^{-1}, \quad \gamma_{c,v} = 1.00 \times 10^{-7}\,(\mathrm{Pa\,s})^{-1}.$$

The coefficients $\tilde{\gamma}_{j,i}$ are given by the value of the reflection coefficient $\sigma_{\mathrm{reflect},ij}$ and the equation

$$\tilde{\gamma}_{j,i}^{\,^{14}\text{C-inulin}} = \gamma_{j,i}(1 - \sigma_{\mathrm{reflect},ij}^{\,^{14}\text{C-inulin}}). \tag{21}$$

We also define the hydraulic permeability of the fluid at the pial surface to define the Robin boundary conditions. Therefore, we search the 3D coefficients $\gamma_{i,j}$ using the previous method and we then compute the hydraulic conductivity L_{ij} that we can use in the definition of the boundary conditions. We assume that the boundary permeability for the ECS compartment is given by a resistance coefficient that we assume to be twice larger than the resistance coefficient of the PVS of arteries, *i.e.* $R_{e,SAS} = 2 \times R_{pa}$. Then, using the relation

$$L_{i,j} = \frac{1}{R_{i,j}\,|S_{i,j}|},$$

where $|S_{i,j}|$ corresponds to the surface area of the pial membrane of the human brain ($\approx 1750 \times 10^2\,\mathrm{mm}^2$), we obtain

$$L_{e,\mathrm{SAS}} = 3.13 \times 10^{-7}\,\mathrm{mm/(Pas)}, \quad L_{pa,\mathrm{SAS}} = 1.25 \times 10^{-6}\,\mathrm{mm/(Pas)}.$$

The next coefficient to define is $\lambda_{i,j}$ for the mass transfer of the solute. Following the definition of diffusive mass transfer, we know that

$$\lambda_{i,j} = P_{i,j} \frac{A_{\text{vessel}}}{V_{\text{tissue}}}, \tag{22}$$

where $P_{i,j}$ is the permeability (in mm/s) between the two compartments.

The diffusive permeabilities are computed using the method from [44], namely for the permeability to the molecule $\alpha = {}^{14}$C-inulin , we have

$$P^{\alpha} = \frac{1}{\pi D_v} \sum_{r \in F} \frac{1}{R_r^{\alpha}},$$

where D_v corresponds to the diameter of the considered vessel (10×10^{-3} mm for capillaries [23], 50×10^{-3} for arterioles and venules [51, 52]), F is the set of index corresponding to the different layers of the membrane for which we compute the permeability, R_r^{α} is the resistances to solute transport for the different layers. For the AEF barrier, the only layer to cross is the astrocyte endfeet processes. We have the definition of the resistance

$$R_{\text{AEF}} = \frac{L_{\text{AEF}}}{2B_{\text{AEF}} D_{\text{AEF}}^{\alpha}},$$

where L_{AEF} is the width of the membrane, $2B_{\text{AEF}}$ is the width between two astrocyte endfeet, and D_{AEF}^{α} is the diffusion coefficient in this same cleft. Assuming that the cleft has a cylindrical shape, the latter parameter is assumed to be given from the relation [48]

$$\begin{cases} D_{\text{AEF}}^{\alpha} = D_{\text{free}}^{\alpha} \left(1 - 2.10444\beta + 2.08877\beta^3 - 0.094813\beta^5 - 1.372\beta^6\right), \\ \alpha = \frac{a^{\alpha}}{B_{\text{AEF}}}, \end{cases}$$

in which a is the solute radius. The Stokes radius of inulin is indicated to be $a^{\text{Inulin}} = 15.2 \times 10^{-7}$ mm in [65].

The permeabilities are computed from the method in [44]. For ^{14}C-inulin , we have

$$\lambda_{pa,e}^{{}^{14}\text{C-inulin}} = 5.98 \times 10^{-5}\,\text{s}^{-1}, \quad \lambda_{pv,e}^{{}^{14}\text{C-inulin}} = 5.97 \times 10^{-5}\,\text{s}^{-1}, \quad \lambda_{pc,e}^{{}^{14}\text{C-inulin}} = 3.63 \times 10^{-5}\,\text{s}^{-1}.$$

A.3 Variations of PVS porosities

In our article, we assumed some variations of the PVSs volume. Using the resistance formula provided in [77] which gives

$$R \propto \frac{1}{r_1^4},$$

where r_1 is the inner radius of the PVS. Thus, with our equation for the permeability coefficient (19), we obtain the proportionality relation

$$\kappa_j \propto r^4.$$

Furthermore, assuming that the PVSs are just holed cylinders, the change of volume is proportional to the change in r_1^2. Therefore, from the two previous proportionality relations, we obtain the multiplying the volume of the PVS by a constant C results in multiplying the permeability by the square of this constant.

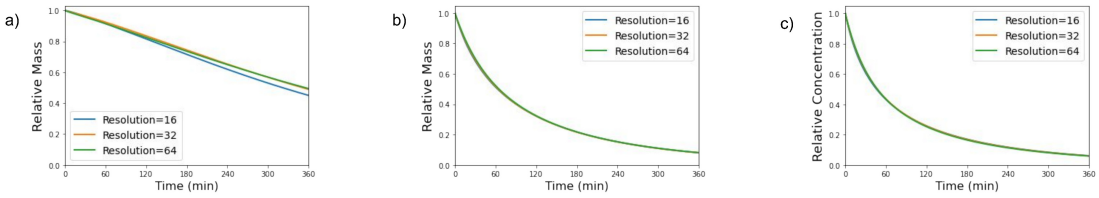

Figure 8: The evolution of tracer measurements relative to the initial value, plotted for varying mesh resolution. The simulations were run for a pure diffusion model using the tracer decay model and a time step of 1 minute. a) Relative mass within the entire brain. b) Relative mass within a cube with side lengths 2mm. c) Relative concentration at the injection point.

B Varying Mesh Resolution and Time Steps

This appendix illustrates the effect of the mesh resolution and the size of time steps on the results of the simulations presented throughout this paper. Following the procedure from Section 2.6, we create different meshes of varying resolution. The smallest and largest cell size corresponding to each of the resolutions are listed in Table 6. For each of these meshes, we simulate a pure

Resolution	h_{min}	h_{max}
16	0.265	2.374
32	0.154	1.190
64	0.073	0.622

Table 6: The smallest and largest cell size h of the mesh for different values of the resolution argument provided to SVMTK.

diffusion model to investigate the impact of mesh resolution on different tracer measurements of interest. Results can be found in Fig 8. We observe a slight difference between the clearance curves obtained from the mesh with resolution 16 and the mesh with resolution 32. However, the clearance curves obtained from the 64- and the 32-resolution mesh are virtually indistinguishable. We conclude that our scheme converges for the pure diffusion model and the mesh with resolution 32 produces accurate results.

Similarly, we investigate the impact of varying the time step sizes on the clearance curves. The results are shown in in Fig 9 and illustrate that a time step of $\delta t = 60$ seconds as used in our simulations is sufficiently accurate.

Next, we plot the clearance curves for the 7-compartment model for both varying mesh resolutions and time step size in Fig 10. The behaviour for the full model is similar to the pure diffusion model, and indicate that further refining the mesh or reducing the time steps will have minimal impact on the clearance curves, especially if we compare it to the uncertainty in other parameters.

Finally, we study the convergence properties of the numerical method for solving the pressure equations. We use the solution of the 64-resolution mesh as a reference solution and compute the L^2 and H^1 error norm with the solutions for the different mesh refinement levels. We obtain the results stated in Table 7 for second-order Lagrange polynomials.

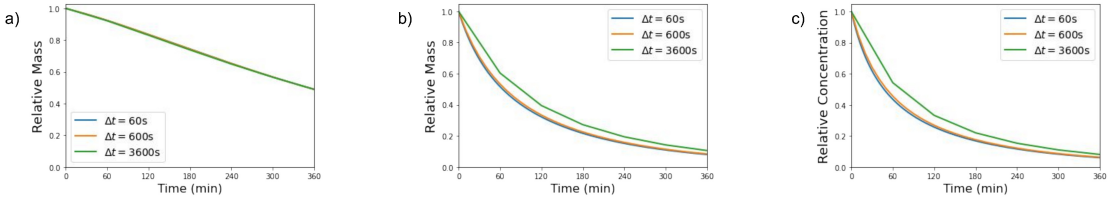

Figure 9: The evolution of tracer measurements relative to the initial value in the pure diffusion model, plotted for varying time step sizes. The simulations were done using the tracer decay model and a mesh with resolution 32. a) Relative mass within the entire brain. b) Relative mass within a cube with side lengths 2mm. c) Relative concentration at the injection point.

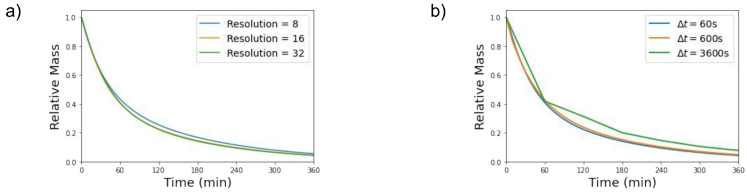

Figure 10: The evolution of total tracer mass relative to the initial value in the 7-compartment model, plotted for a) varying mesh resolution (with a timestep of 60s) and b) varying time step sizes (with mesh resolution 32).

Resolution	L^2-error norm	order	H^1-error norm	order
8	748		2302	
16	404	0.89	1659	0.47
32	82	2.29	851	0.96

Table 7: Computed L^2 and H^1 error norms and convergence orders for our numerical method to solve the pressure equation of the multi-compartment model using second order Lagrange elements

References

[1] N. J. Abbott, M. E. Pizzo, J. E. Preston, D. Janigro, and R. G. Thorne, *The role of brain barriers in fluid movement in the CNS: is there a 'glymphatic' system?*, Acta Neuropathol, 135 (2018), pp. 387–407.

[2] P. Alliez, C. Jamin, L. Rineau, S. Tayeb, J. Tournois, and M. Yvinec, *3D mesh generation*, in CGAL User and Reference Manual, CGAL Editorial Board, 5.4 ed., 2022.

[3] M. S. Alnæs, J. Blechta, J. E. Hake, A. Johansson, B. Kehlet, A. Logg, C. Richardson, J. Ring, M. E. Rognes, and G. N. Wells, *The fenics project version 1.5*, Archive of Numerical Software, 3 (2015).

[4] M. Asgari, D. de Zélicourt, and V. Kurtcuoglu, *Glymphatic solute transport does not require bulk flow*, Sci Rep, 6 (2016), p. 38635. Number: 1 Publisher: Nature Publishing Group.

[5] M. Bai, D. Elsworth, and J.-C. Roegiers, *Multiporosity/multipermeability approach to the simulation of naturally fractured reservoirs*, Water Resources Research, 29 (1993), pp. 1621–1633.

[6] ——, *Multiporosity/multipermeability approach to the simulation of naturally fractured reservoirs*, Water Resources Research, 29 (1993), pp. 1621–1633.

[7] E. N. Bakker, D. M. Naessens, and E. VanBavel, *Paravascular spaces: entry to or exit from the brain?*, Experimental physiology, 104 (2019), pp. 1013–1017.

[8] L. Ballerini, T. Booth, M. del C. Valdés Hernández, S. Wiseman, R. Lovreglio, S. Muñoz Maniega, Z. Morris, A. Pattie, J. Corley, A. Gow, M. E. Bastin, I. J. Deary, and J. Wardlaw, *Computational quantification of brain perivascular space morphologies: Associations with vascular risk factors and white matter hyperintensities. a study in the lothian birth cohort 1936*, NeuroImage: Clinical, 25 (2020), p. 102120.

[9] B. Bedussi, M. Almasian, J. de Vos, E. VanBavel, and E. N. Bakker, *Paravascular spaces at the brain surface: Low resistance pathways for cerebrospinal fluid flow*, Journal of Cerebral Blood Flow & Metabolism, 38 (2018), pp. 719–726. PMID: 29039724.

[10] M. A. Biot, *General theory of three-dimensional consolidation*, Journal of Applied Physics, 12 (1941), pp. 155–164.

[11] M. A. Biot, *Theory of elasticity and consolidation for a porous anisotropic solid*, Journal of Applied Physics, 26 (1955), pp. 182–185.

[12] I. Bloomfield, I. Johnston, and L. Bilston, *Effects of proteins, blood cells and glucose on the viscosity of cerebrospinal fluid*, Pediatric neurosurgery, 28 (1998), pp. 246–251.

[13] L. Bojarskaite, D. M. Bjørnstad, A. Vallet, K. M. G. Binder, C. Cunen, K. Heuser, M. Kuchta, K.-A. Mardal, and R. Enger, *Sleep cycle-dependent vascular dynamics enhance perivascular cerebrospinal fluid flow and solute transport*, bioRxiv, (2022).

[14] M. Croci, V. Vinje, and M. E. Rognes, *Uncertainty quantification of parenchymal tracer distribution using random diffusion and convective velocity fields*, Fluids and Barriers of the CNS, 16 (2019), pp. 1–21.

[15] H. F. Cserr, M. DePasquale, C. Nicholson, C. S. Patlak, K. D. Pettigrew, and M. E. Rice, *Extracellular volume decreases while cell volume is maintained by ion uptake in rat brain during acute hypernatremia.*, The Journal of Physiology, 442 (1991), pp. 277–295.

[16] H. F. Cserr, C. J. Harling-Berg, and P. M. Knopf, *Drainage of brain extracellular fluid into blood and deep cervical lymph and its immunological significance*, Brain pathology, 2 (1992), pp. 269–276.

[17] C. D'angelo and A. Quarteroni, *On the coupling of 1d and 3d diffusion-reaction equations: application to tissue perfusion problems*, Mathematical Models and Methods in Applied Sciences, 18 (2008), pp. 1481–1504.

[18] W. El-Bouri, Y. Bing, T. Józsa, and S. Payne, *A novel multi-scale, multi-compartment model of oxygen transport - towards in-silico clinical trials in the entire human brain*, 09 2019.

[19] W. K. El-Bouri, A. MacGowan, T. I. Józsa, M. J. Gounis, and S. J. Payne, *Modelling the impact of clot fragmentation on the microcirculation after thrombectomy*, PLOS Computational Biology, 17 (2021), pp. 1–25.

[20] W. K. El-Bouri and S. J. Payne, *Multi-scale homogenization of blood flow in 3-dimensional human cerebral microvascular networks*, Journal of theoretical biology, 380 (2015), pp. 40–47.

[21] E. Eliseussen, M. E. Rognes, and T. B. Thompson, *A-posteriori error estimation and adaptivity for multiple-network poroelasticity*, arXiv preprint arXiv:2111.13456, (2021).

[22] K. Erbertseder, J. Reichold, B. Flemisch, P. Jenny, and R. Helmig, *A coupled discrete/continuum model for describing cancer-therapeutic transport in the lung*, PLOS ONE, 7 (2012), pp. 1–17.

[23] E. Farkas and P. G. Luiten, *Cerebral microvascular pathology in aging and alzheimer's disease*, Progress in Neurobiology, 64 (2001), pp. 575–611.

[24] A. Fedorov, R. Beichel, J. Kalpathy-cramer, J. Finet, J. christophe Fillion-robin, S. Pujol, C. Bauer, D. Jennings, F. Fennessy, M. Sonka, J. Buatti, S. Aylward, J. V. Miller, S. Pieper, and R. Kikinis, *3d slicer as an image computing platform for the quantitative imaging network*, Magnetic Resonance Imaging, 30 (2012), pp. 1323–1341.

[25] P. Fraser, A. D. Dallas, and S. Davies, *Measurement of filtration coefficient in single cerebral microvessels of the frog.*, The Journal of physiology, 423 (1990), pp. 343–361.

[26] L. Guo, Z. Li, J. Lyu, Y. Mei, J. C. Vardakis, D. Chen, C. Han, X. Lou, and Y. Ventikos, *On the validation of a multiple-network poroelastic model using arterial spin labeling mri data*, Frontiers in Computational Neuroscience, 13 (2019).

[27] L. Guo, J. C. Vardakis, T. Lassila, M. Mitolo, N. Ravikumar, D. Chou, M. Lange, A. Sarrami-Foroushani, B. J. Tully, Z. A. Taylor, S. Varma, A. Venneri, A. F. Frangi, and Y. Ventikos, *Subject-specific multi-poroelastic model for exploring the risk factors associated with the early stages of alzheimer's disease*, Interface Focus, 8 (2018), p. 20170019.

[28] M. J. Hernández, R. W. Brennan, and G. S. Bowman, *Cerebral blood flow autoregulation in the rat.*, Stroke, 9 (1978), pp. 150–154.

[29] K. E. Holter, B. Kehlet, A. Devor, T. J. Sejnowski, A. M. Dale, S. W. Omholt, O. P. Ottersen, E. A. Nagelhus, K.-A. Mardal, and K. H. Pettersen, *Interstitial solute transport in 3d reconstructed neuropil occurs by diffusion rather than bulk flow*, Proceedings of the National Academy of Sciences, 114 (2017), pp. 9894–9899.

[30] M. Hornkjol, L. M. Valnes, G. Ringstad, M. E. Rognes, P. K. Eide, K.-A. Mardal, and V. Vinje, *Csf circulation and dispersion yield rapid clearance from intracranial compartments*, bioRxiv, (2022).

[31] U. Hornung, ed., *Homogenization and Porous Media*, Springer-Verlag, Berlin, Heidelberg, 1996.

[32] J. J. Iliff, M. Wang, Y. Liao, B. A. Plogg, W. Peng, G. A. Gundersen, H. Benveniste, G. E. Vates, R. Deane, S. A. Goldman, E. A. Nagelhus, and M. Nedergaard, *A paravascular pathway facilitates csf flow through the brain parenchyma and the clearance of interstitial solutes, including amyloid β*, Science Translational Medicine, 4 (2012), pp. 147ra111–147ra111.

[33] M. Jarzyńska, *The application of practical kedem-katchalsky equations in membrane transport*, Central European Journal of Physics, 4 (2006), pp. 429–438.

[34] N. A. Jessen, A. S. F. Munk, I. Lundgaard, and M. Nedergaard, *The Glymphatic System: A Beginner's Guide*, Neurochem Res, 40 (2015), pp. 2583–2599.

[35] T. I. Józsa, R. M. Padmos, N. Samuels, W. El-Bouri, A. G. Hoekstra, and S. J. Payne, *A porous circulation model of the human brain for in silico clinical trials in ischaemic stroke*, Interface Focus, 11 (2021), p. 20190127.

[36] L. JR, *Capillary filtration-absorption balance reconsidered in light of dynamic extravascular factors*, Experimental Physiology, 76 (1991), pp. 825–857.

[37] M. Kimura, H. H. Dietrich, V. H. Huxley, D. R. Reichner, and R. G. Dacey, *Measurement of hydraulic conductivity in isolated arterioles of rat brain cortex*, American Journal of Physiology-Heart and Circulatory Physiology, 264 (1993), pp. H1788–H1797. PMID: 8322907.

[38] H. Kleven, I. Bjerke, J. Imad, F. Clasca, H. Groenewegen, J. Bjaalie, and T. Leergaard, *WHS rat brain atlas v4*. In preparation.

[39] Y. Lai, P. Smith, W. Lamm, and J. Hildebrandt, *Sampling and analysis of cerebrospinal fluid for chronic studies in awake rats*, Journal of Applied Physiology, 54 (1983), pp. 1754–1757.

[40] R. C. Lanman, J. A. Burton, and L. S. Schanker, *Diffusion coefficients of some 14c-labeled saccharides of biological interest*, Life Sciences, 10 (1971), pp. 803–811.

[41] S.-P. Lee, T. Q. Duong, G. Yang, C. Iadecola, and S.-G. Kim, *Relative changes of cerebral arterial and venous blood volumes during increased cerebral blood flow: Implications for bold fmri*, Magnetic Resonance in Medicine, 45 (2001), pp. 791–800.

[42] G. Li, M. J. Simon, L. M. Cancel, Z.-D. Shi, X. Ji, J. M. Tarbell, B. Morrison, and B. M. Fu, *Permeability of endothelial and astrocyte cocultures: in vitro blood–brain barrier models for drug delivery studies*, Annals of biomedical engineering, 38 (2010), pp. 2499–2511.

[43] G. Li, W. Yuan, and B. M. Fu, *A model for the blood–brain barrier permeability to water and small solutes*, Journal of Biomechanics, 43 (2010), pp. 2133–2140.

[44] ——, *A model for the blood–brain barrier permeability to water and small solutes*, Journal of Biomechanics, 43 (2010), pp. 2133–2140.

[45] A. Logg, K.-A. Mardal, G. N. Wells, et al., *Automated Solution of Differential Equations by the Finite Element Method*, Springer, 2012.

[46] K.-A. Mardal, M. Rognes, T. Thompson, and L. Valnes, *Mathematical Modeling of the Human Brain: From Magnetic Resonance Images to Finite Element Simulation*, Springer, Cham, 01 2022.

[47] H. Mestre, J. Tithof, T. Du, W. Song, W. Peng, A. M. Sweeney, G. Olveda, J. H. Thomas, M. Nedergaard, and D. H. Kelley, *Flow of cerebrospinal fluid is driven by arterial pulsations and is reduced in hypertension*, Nat Commun, 9 (2018), p. 4878. Number: 1 Publisher: Nature Publishing Group.

[48] C. C. Michel and F. E. Curry, *Microvascular permeability*, Physiological Reviews, 79 (1999), pp. 703–761. PMID: 10390517.

[49] E. R. Muir, Q. Shen, and T. Q. Duong, *Cerebral blood flow mri in mice using the cardiac-spin-labeling technique*, Magnetic Resonance in Medicine, 60 (2008), pp. 744–748.

[50] L. A. Murtha, Q. Yang, M. W. Parsons, C. R. Levi, D. J. Beard, N. J. Spratt, and D. D. McLeod, *Cerebrospinal fluid is drained primarily via the spinal canal and olfactory route in young and aged spontaneously hypertensive rats*, Fluids and Barriers of the CNS, 11 (2014), pp. 1–9.

[51] A. C. Ngai and H. R. Winn, *Modulation of cerebral arteriolar diameter by intraluminal flow and pressure*, Circulation Research, 77 (1995), pp. 832–840.

[52] J. Nguyen, N. Nishimura, R. N. Fetcho, C. Iadecola, and C. B. Schaffer, *Occlusion of cortical ascending venules causes blood flow decreases, reversals in flow direction, and vessel dilation in upstream capillaries*, Journal of Cerebral Blood Flow & Metabolism, 31 (2011), pp. 2243–2254. PMID: 21712834.

[53] C. Nicholson and J. M. Phillips, *Ion diffusion modified by tortuosity and volume fraction in the extracellular microenvironment of the rat cerebellum.*, The Journal of Physiology, 321 (1981), pp. 225–257.

[54] D. Orešković and M. Klarica, *The formation of cerebrospinal fluid: Nearly a hundred years of interpretations and misinterpretations*, Brain Research Reviews, 64 (2010), pp. 241–262.

[55] E. A. Papp, T. B. Leergaard, E. Calabrese, G. A. Johnson, and J. G. Bjaalie, *Waxholm space atlas of the sprague dawley rat brain*, NeuroImage, 97 (2014), pp. 374–386.

[56] W. M. Pardridge, *Drug transport in brain via the cerebrospinal fluid*, Fluids and Barriers of the CNS, 8 (2011), pp. 1–4.

[57] R. Penta, D. Ambrosi, and A. Quarteroni, *Multiscale homogenization for fluid and drug transport in vascularized malignant tissues*, Mathematical Models and Methods in Applied Sciences, 25 (2015), pp. 79–108.

[58] A. T. Perles-Barbacaru and H. Lahrech, *A new magnetic resonance imaging method for mapping the cerebral blood volume fraction: The rapid steady-state t1 method*, Journal of Cerebral Blood Flow & Metabolism, 27 (2007), pp. 618–631. PMID: 16850031.

[59] S. T. Proulx, *Cerebrospinal fluid outflow: a review of the historical and contemporary evidence for arachnoid villi, perineural routes, and dural lymphatics*, Cellular and Molecular Life Sciences, 78 (2021), pp. 2429–2457.

[60] L. Ray, J. J. Iliff, and J. J. Heys, *Analysis of convective and diffusive transport in the brain interstitium*, Fluids Barriers CNS, 16 (2019), pp. 1–18. Number: 1 Publisher: BioMed Central.

[61] L. A. Ray, M. Pike, M. Simon, J. J. Iliff, and J. J. Heys, *Quantitative analysis of macroscopic solute transport in the murine brain*, Fluids and Barriers of the CNS, 18 (2021), pp. 1–19.

[62] B. C. Reeves, J. K. Karimy, A. J. Kundishora, H. Mestre, H. M. Cerci, C. Matouk, S. L. Alper, I. Lundgaard, M. Nedergaard, and K. T. Kahle, *Glymphatic System Impairment in Alzheimer's Disease and Idiopathic Normal Pressure Hydrocephalus*, Trends in Molecular Medicine, 26 (2020), pp. 285–295. Publisher: Elsevier.

[63] T. J. Roberts, A. C. Chapman, and M. J. Cipolla, *Ppar-γ agonist rosiglitazone reverses increased cerebral venous hydraulic conductivity during hypertension*, American Journal of Physiology-Heart and Circulatory Physiology, 297 (2009), pp. H1347–H1353.

[64] U. Roy Chowdhury, B. H. Holman, and M. P. Fautsch, *A novel rat model to study the role of intracranial pressure modulation on optic neuropathies*, PLOS ONE, 8 (2013), p. null.

[65] S. G. Schultz and A. K. Solomon, *Determination of the Effective Hydrodynamic Radii of Small Molecules by Viscometry* , Journal of General Physiology, 44 (1961), pp. 1189–1199.

[66] L. Shi, M. Zeng, Y. Sun, and B. M. Fu, *Quantification of Blood-Brain Barrier Solute Permeability and Brain Transport by Multiphoton Microscopy*, Journal of Biomechanical Engineering, 136 (2014). 031005.

[67] R. J. Shipley and S. J. Chapman, *Multiscale Modelling of Fluid and Drug Transport in Vascular Tumours*, Bull. Math. Biol., 72 (2010), pp. 1464–1491.

[68] R. J. Shipley, P. W. Sweeney, S. J. Chapman, and T. Roose, *A four-compartment multiscale model of fluid and drug distribution in vascular tumours*, International Journal for Numerical Methods in Biomedical Engineering, 36 (2020), p. e3315.

[69] A. J. Smith and A. S. Verkman, *Going against the flow: Interstitial solute transport in brain is diffusive and aquaporin-4 independent*, The Journal of physiology, 597 (2019), p. 4421.

[70] J. H. Smith and J. A. Humphrey, *Interstitial transport and transvascular fluid exchange during infusion into brain and tumor tissue*, Microvascular research, 73 (2007), pp. 58–73.

[71] K. H. Støverud, M. Darcis, R. Helmig, and S. M. Hassanizadeh, *Modeling Concentration Distribution and Deformation During Convection-Enhanced Drug Delivery into Brain Tissue*, Transp Porous Med, 92 (2012), pp. 119–143.

[72] J. Tithof, K. A. Boster, P. A. Bork, M. Nedergaard, J. H. Thomas, and D. H. Kelley, *A network model of glymphatic flow under different experimentally-motivated parametric scenarios*, iScience, 25 (2022), p. 104258.

[73] C. Trainor and M. Silverman, *Transcapillary exchange of molecular weight markers in the postglomerular circulation: application of a barrier-limited model*, American Journal of Physiology-Renal Physiology, 242 (1982), pp. F436–F446.

[74] B. TULLY and Y. VENTIKOS, *Cerebral water transport using multiple-network poroelastic theory: application to normal pressure hydrocephalus*, Journal of Fluid Mechanics, 667 (2011), p. 188–215.

[75] L. M. Valnes, S. K. Mitusch, G. Ringstad, P. K. Eide, S. W. Funke, and K.-A. Mardal, *Apparent diffusion coefficient estimates based on 24 hours tracer movement support glymphatic transport in human cerebral cortex*, Sci Rep, 10 (2020), p. 9176.

[76] J. C. Vardakis, D. Chou, B. J. Tully, C. C. Hung, T. H. Lee, P.-H. Tsui, and Y. Ventikos, *Investigating cerebral oedema using poroelasticity*, Medical Engineering & Physics, 38 (2016), pp. 48–57. Micro and Nano Flows 2014 (MNF2014) - Biomedical Stream.

[77] V. Vinje, A. Eklund, K.-A. Mardal, M. E. Rognes, and K.-H. Støverud, *Intracranial pressure elevation alters csf clearance pathways*, Fluids and Barriers of the CNS, 17 (2020).

[78] J. Waters, *The concentration of soluble extracellular amyloid-β protein in acute brain slices from crnd8 mice*, PLOS ONE, 5 (2011), pp. 1–16.

[79] H. Wiig and R. K. Reed, *Rat brain interstitial fluid pressure measured with micropipettes*, American Journal of Physiology-Heart and Circulatory Physiology, 244 (1983), pp. H239–H246. PMID: 6401940.

[80] L. Xie, H. Kang, Q. Xu, M. J. Chen, Y. Liao, M. Thiyagarajan, J. O'Donnell, D. J. Christensen, C. Nicholson, J. J. Iliff, T. Takano, R. Deane, and M. Nedergaard, *Sleep drives metabolite clearance from the adult brain*, Science, 342 (2013), pp. 373–377.